THE UNIVERSITY OF CALIFORNIA,
IRVINE

Integrated Stretchable Circuits and Machine Learning for Human Vital Signs Monitoring

DISSERTATION

submitted in partial satisfaction of the requirements
for the degree of

DOCTOR OF PHILOSOPHY

in Biomedical Engineering

by

Yongxiao Zhou

Dissertation Committee:
Professor Michelle Khine, Chair
Professor Jim Brody
Professor Elliot Hui
Professor Amir Rahmani

2023

DEDICATION

To:

My friends and family for their continual support and encouragement through this journey

TABLE OF CONTENTS

	Page
LIST OF FIGURES	iv
ACKNOWLEDGMENTS	v
VITA	vi
ABSTRACT OF THE DISSERTATION	vii
INTRODUCTION	1
CHAPTER 1: Introduction and Requirements for Stretchable Wearable Electronics	4
CHAPTER 2: Design and Fabrication of Stretchable Electronics' Substrate	11
CHAPTER 3: High-Resolution Integrated Piezoresistive Sensors for Microfluidic Monitoring	17
CHAPTER 4: Surface Mount Devices and Integration Method with Stretchable Circuit	40
CHAPTER 5: Sleep Data Analysis and Machine Learning	51
CHAPTER 6: Discussion and Future Prospect	71
REFERENCES	75

LIST OF FIGURES

	Page
Figure 0	3
Figure 1	26
Figure 2	29
Figure 3	33
Figure 4	42
Figure 5	45
Figure 6	46
Figure 7	48
Figure 8	56
Figure 9	59
Figure 10	60
Figure 11	63
Figure 12	64

ACKNOWLEDGMENTS

I want to convey my heartfelt appreciation to Professor Michelle Khine for continually presenting me with new challenges and enabling me to develop as an individual and a researcher under her tutelage. Through her mentorship, I have had the opportunity to engage in work that I never thought possible, and I am truly grateful for her support and leadership. Furthermore, I would like to express my gratitude to my committee members, Professor Jim Brody, Professor Elliot Hui, and Professor Amir Rahmani, for their careful review of my graduate work and for providing me with guidance throughout my academic journey at U.C. Irvine. Thank you for your invaluable feedback and mentorship.

I would like to express my gratitude to my friends and family for their unwavering support over the past five years. I am grateful for the times they took me away from the laboratory and showed me that there is more to life than just my research. I also want to acknowledge my wife, Sara Gao, who has been a constant source of love and support for me over the last seven years. I always knew that I could rely on her at any time of the day, and I thank her for being such an important part of my life.

I owe a debt of gratitude to my current and former labmates and classmates for their immense support throughout my journey. Without their contributions, I would not have been able to accomplish what I have today. I extend my heartfelt appreciation to all the undergraduate students who worked tirelessly with me on my research; their hard work has been instrumental in achieving the results presented in this dissertation. I feel fortunate to have been part of a working environment that I looked forward to being in every day.

Lastly, the text of this dissertation is a reprint of the material as it appears in Zhou et al.[1] , used with permission from Royal Society of Chemistry. The co-authors listed in this publication are Erik Werner, Eugene Lee, Michael Chu, Thao Nguyen, Kevin Costa, Elliot Hui, and Michelle Khine.

VITA

Yongxiao Zhou

EDUCATION

2017 B.S. in Biomedical Engineering and Material Science Engineering, University of California, Irvine

2021 M.S. in Biomedical Engineering, University of California, Irvine

2023 Ph.D. in Biomedical Engineering, University of California, Irvine

POSITIONS

2017 - 2023 Graduate Student Researcher, Khine Lab, University of California, Irvine

FIELD OF STUDY

Integrated Stretchable Circuits and Machine Learning for Human Vital Signs Monitoring

PUBLICATION

Yongxiao Zhou, Arash Abiri, Rami Khyat, Michelle Khine. Multi-modalities Machine Learning for Sleep Stage Detection. *In preparation*

Yongxiao Zhou, Chengyang Qian, Arash Abiri, Michael Chu, Patrick Rwei, Michelle Khine. Integrated Stretchable Circuits for Human Vital Signs Monitoring. *In preparation*

Yongxiao Zhou, Erik M Werner, Eugene Lee, Michael Chu, Thao Nguyen, Kevin D Costa, Elliot E Hui, and Michelle Khine. 2021. "High-Resolution Integrated Piezoresistive Sensors for Microfluidic Monitoring." Lab on a Chip 21 (1): 83–92.

Chu, Michael, Thao Nguyen, Vaibhav Pandey, **Yongxiao Zhou**, Hoang N. Pham, Ronen Bar-Yoseph, Shlomit Radom-Aizik, Ramesh Jain, Dan M. Cooper, and Michelle Khine. 2019. "Respiration Rate and Volume Measurements Using Wearable Strain Sensors." Npj Digital Medicine 2 (1): 8.

Qu, Yueqiao, Youmin He, Arya Saidi, Yihang Xin, **Yongxiao Zhou**, Jiang Zhu, Teng Ma, et al. 2018. "In Vivo Elasticity Mapping of Posterior Ocular Layers Using Acoustic Radiation Force Optical Coherence Elastography." Investigative Opthalmology & Visual Science 59 (1): 455.

ABSTRACT OF THE DISSERTATION

Integrated Stretchable Circuits and Machine Learning for Human Vital Signs Monitoring

By

Yongxiao Zhou

Doctor of Philosophy in Biomedical Engineering

University of California, Irvine, 2023

Professor Michelle Khine Irvine, Chair

In the medical field, there is a growing interest in continuous health monitoring as it has the potential to enhance the diagnosis and treatment of patients. However, to be effective, continuous monitoring systems need to be comfortable for patients to wear and able to gather reliable and actionable data. This often requires the device to be soft and conformal to ensure patient comfort and to provide a stable interface for high-quality signal acquisition. While wearable technology and global connectivity have experienced significant growth over the last few decades, progress in stretchable wearable electronics has been slower. This study focuses on developing a systematic and scalable approach to fabricate stretchable wearable systems for monitoring human vital signs. The research employs laser ablation to create stretchable substrates and integrates conventional surface mounted devices (SMD) with stretchable substrates. Lastly, a machine learning method is introduced to analyze vital signs collected from patients during sleep studies. The prediction of sleep stages and events is highly accurate, and there is great potential for conducting at-home sleep studies.

Introduction

In recent decades, wearable electronics have garnered significant interest with advancements in technology and medicine. These devices have evolved to become smaller in size, more sophisticated in function, and more affordable to the general public. Wearable electronics have also found extensive use in the medical field, not only due to their compactness and convenience but also because they are reliable for continuous monitoring. For instance, in the past, patients had to travel to hospitals and undergo electrocardiogram tests using wires, leads, and bulky acquisition instruments. However, with the advent of wearable smartwatches, users can now obtain meaningful EKG signals at any location of their choosing.

Patients now typically only are seen by a care provider on a fixed schedule or when experiencing disease symptoms. This may lead to a delayed or improper diagnosis, particularly for chronic conditions requiring constant monitoring[2]. For instance, if asthma patients exhibit active symptoms but are not treated promptly, the consequences can be dire[3]. Continuous monitoring of vital signals can aid in diagnosing ailments and provide real-time warnings of potential acute symptoms.

Despite the availability of commercialized wearable devices that can measure multiple vital signals, most of them are limited to capturing vital signals for short periods of time, providing only snap shots in time or, at best, small portions of continuous monitoring. Moreover, due to the rigid nature of traditional sensors, such as those found in Apple watches, they are only capable of measuring certain types of vital signals, such as pulse, blood oxygen, and EKG[4]. Other vital signals, such as blood pressure and respiration, are difficult to measure with stiff devices. Conversely, the common sphygmomanometer has a soft and inflatable bladder, and a stretchable respiratory inductance plethysmography band can be used to measure the expansion of the ribcage or abdomen; however, they are bulky and cannot provide continuous monitoring. Therefore, there is significant interest and

effort in developing more advanced wearable sensing systems capable of continuously measuring other important vital signals[5].

Stretchable electronics have become a crucial branch of wearable sensors. They have attracted significant interest in recent years due to the growing demand for more versatile and functional wearable electronics[6–8], healthcare monitoring[9–11], and microfluidic systems[1,12]. Unlike traditional electronic circuits, which can be rigid and unsuited for soft anatomy such as human skin, stretchable electronics are flexible and can be stretched to a certain threshold, allowing them to conform to soft surfaces. This improved conformability not only enhances user comfort but also enables high-quality signal acquisition in dynamic environments such as during movement or exercise. Using stretchable materials also allows for the acquisition of vital signals that are difficult to capture using rigid electronics.

Another important consideration is how to process the signals collected by wearable devices. While developing reliable devices is essential, limited information can be extracted from the data without proper analysis. Traditional signal analysis methods are effective for some tasks but may be unreliable when replacing well-trained professionals in decision-making. However, with the advancement of computational power and artificial intelligence, integrating big data and machine learning can help make more efficient and accurate healthcare decisions. By applying appropriate machine learning algorithms to collected vital signals, efficiency can be increased, and bias can be decreased. In some applications, artificial intelligence outperforms humans when data is processed, and models are trained correctly.

This dissertation will focus on developing and applying a soft, stretchable circuit board platform, which can be used to create multi-modality wearable devices. The general topics' relationship is described in figure 0. Chapter 1 is the introduction and background of the entire dissertation. Chapters 2, 3, and 4 will delve into the main topic, with Chapter 2 discussing the electrode architecture and

stretchable substrate, Chapter 3 covers the development of a super sensitive stretchable sensor that inspired the creation of the stretchable circuit board, and Chapter 4 details the applications of the stretchable circuit board. Chapter 5 focuses on signal processing and algorithms for utilizing the collected signals, specifically machine learning techniques for analyzing vital signals collected from sleeping patients. This approach can be extended to other vital signals for predictive analysis. Finally, Chapter 6 will discuss future work, identifying ways to improve existing devices and broaden their potential applications.

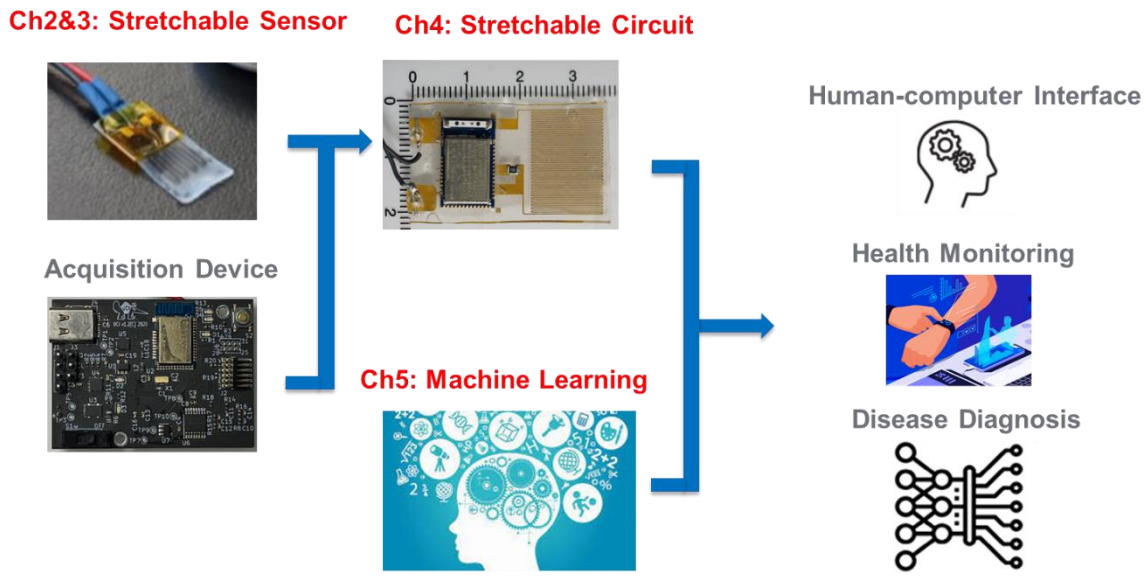

Fig. 0 Relationship among different chapters in this dissertation

Chapter 1: Introduction and Requirements for Stretchable Wearable Electronics

Compared to traditional sensors that consist of stiff materials, soft and stretchable electronics offer numerous benefits and can be applied to a range of applications, such as human wearable devices, to achieve better performance. However, due to a stiffness mismatch, PCBs (Printed Circuit Boards) may not attach well to the skin under dynamic conditions, causing relative movement between the skin and the device and leading to decreased signal acquisition quality. An alternative approach is to apply extra pressure and adhesive to reduce the relative movement at the interface. However, this may cause patients to feel more uncomfortable and even affect normal blood flow and other vital activities.

In this chapter, we will review the criteria for wearable electronics and explore state-of-the-art technology.

1.1: Introduction and Motivation

The first and most important criteria for wearable electronics are safety and biocompatibility. Devices that use noble metals are better than those that use liquid or toxic metals, as well as devices that use latex and nickel, which are common allergens. Since users or patients may need to wear these devices for extended periods, comfort is crucial. Smaller and lighter devices are ideal as they are less noticeable. As previously mentioned, stiff wearable devices require extra pressure to be applied to the skin to ensure signal quality, which can be uncomfortable. Therefore, devices that have stiffness and modulus similar to human skin are preferable.

High-quality signals are crucial for acquisition devices. Traditional stiff devices often experience noise and defects due to unstable connections or poor interfaces between the measured surface and the device. However, thin and stretchable wearables can laminate onto the skin and stretch or distort along with the skin, reducing relative movement and creating a stable interface between the device and the skin. To attach the device to the skin, it is necessary to use biocompatible adhesives[13–16]. Signals are generally transmitted from the acquisition device via wires and cables, which are stable and reliable but

not suitable for dynamic systems. Battery-powered and short-range wireless communication systems are widely used for wearable devices. These devices typically transmit data to connected smart devices, such as phones, which can then analyze the data locally or upload it to the cloud. However, wearable devices still require acquisition circuits to measure and pre-process signals before they are transmitted.

Efforts in creating stretchable electronics have focused on two primary approaches: (1) generating stretchable electronic components or (2) integrating rigid components onto stretchable and conductive substrates. In recent years, researchers have made significant advancements in the former approach, developing fully stretchable transistors and capacitors[17–20]. However, this technique is still relatively immature, and its commercial feasibility and capacity for cost-effective mass production have not been well-defined. One major obstacle to the mass production of stretchable electronic components is the lack of specific production lines that are compatible with the required materials. Additionally, these components have lower reliability and shorter lifespans compared to traditional rigid components, which is another issue that must be addressed.

In summary, the safety and biocompatibility of wearable devices and their comfort, size, and weight are all critical factors to consider when developing wearable electronics. By using noble metals and designing devices with similar properties to human skin, we can create comfortable and safe wearable devices that can be used for extended periods without causing discomfort or harm to the wearer.

To achieve high-quality signals, it is important to have a stable and reliable interface between the device and the skin, which can be achieved through stretchable wearables and biocompatible adhesives. Short-range wireless communication systems and batteries are suitable for dynamic systems and can transmit data to connected smart devices. Finally, acquisition circuits are necessary to measure and pre-process signals before transmission.

While progress has been made in developing stretchable electronic components, challenges remain, such as commercial feasibility, cost-effective mass production, and reliability. Addressing these challenges will be crucial to realizing the full potential of stretchable electronics and bringing them to market.

1.2: Current State of Art of Stretchable Electronics

1.2.1: Substrate Layer

Although stretchable electronic circuits have limitations, some of the more attainable techniques for creating them involve integrating rigid electronic components in the form of surface mounted devices (SMDs) onto stretchable substrates. Compared to traditional rigid circuits, these stretchable electronic circuits can bend, twist, and conform with deformable interfaces due to the flexible properties of the elastomeric soft substrate material.

Stretchable circuits typically have a substrate layer, a functional conductive layer, and a component layer consisting of electrical components and interconnects between the functional layer and rigid electrical components[10,21–28]. The conductive functional layer is usually bonded to a polymer-based substrate layer, and additional components are electrically bonded to either the conductive functional layer or substrate layer. Depending on the application, an encapsulation layer may also be added for insulation purposes.

To create these stretchable circuit boards, the substrate layer must be sufficiently stretchable to support other layers and components, and its stretchability determines the device's fracture point. Researchers often use a stretchable elastomer, such as Ecoflex or polydimethylsiloxane (PDMS), to increase the substrate's stretchability as it is easy to use and relatively inexpensive[21–25,28]. Some researchers have also utilized special surface geometry on the substrate layer, such as the Miura-ori structure, to compensate for strain changes when the device is stretched, increasing the overall stretchability of the substrate by 75%[26,27]. However, the choice of materials and structure design affects the complexity and efficiency of fabrication, functionality, lifetime, and other aspects of electronics.

1.2.2: Functional Layer

Besides the substrate layer, the stretchability of the functional layer is also crucial to the overall circuit's flexibility. The conductive functional layer is usually made of metal or conductive organic materials and can be designed differently depending on the material. Planar conductive functional layers usually have poor stretchability; thus, most stretchable electronic devices adopt a serpentine design to ensure performance under high strain[10,14,21,22,25,29]. For example, Xu et al. developed a novel free-floating conductive wire that could buckle, twist, and deform in and out of the plane, which improved the range of stretchability.[14] However, the serpentine free-floating design and liquid suspension add more complexity to the fabrication, take up more space in the circuit, and affect the robustness of the system. It also adds more uncertainty to predicting the failure because of deformation and rotation of the conductive wire happen in the vertical direction. Elastomer-based conductive nanocomposites, which are synthesized by mixing elastomeric matrix and conductive nano-materials at a customized ratio, serve as alternative options to solving this problem[30–33]. These composites are intrinsically conductive and stretchable and have been widely developed by researchers. However, when they are stretched, these nanocomposites suffer significant increases in resistance and are, therefore, mostly used as strain sensors. Indeed, Cho and colleagues attempted to use silver nanoparticle ink as conductive material for SCBs, but the stretchability of the board was limited to 25%[34]. Alternatively, stress-relief wrinkle structures on the conductive functional layer have been shown to increase stretchability and may, therefore, serve as a good candidate[1,9,10,28]. Over the years, researchers have introduced different methods for creating wrinkle structures to accommodate the change in strain once stretched. Their relatively good stretchability and performance also make them a popular choice for stretchable conductive material.

1.2.3: Interconnects

The interconnects are the interface between the functional material and electrical components. Although different types of solder are the mostly wide-used material for interconnects[14,22,25,29], they still possess disadvantages due to their intrinsic stiffness mismatch when applied to soft polymer substrates. Because of the stiffness mismatch, the failure of the integrated electronic during stretching usually occurs at the interconnects and limits the stretchability of the circuit. For example, the wire designed by Lin's group was able to stretch up to 80%; however, when stiff electronic components and interconnects were introduced to the circuit, the stretchability decreased to ~30%[29]. Liquid metal can be an alternative option that avoids the stiffness mismatch problem associated with solder and can also be used as the functional layer to provide good stretchability and performance[21,23]. When liquid metal is used in electronics, the stiffness mismatch and conductivity of the interconnects are no longer a major limiting factor compared to solder, as long as the SMDs are contacting the liquid metal. However, channels that contain liquid metal require extra precautions during fabrication and handling, as they are more prone to mechanical failure. Thus, an alternative to increasing the robustness of the circuit is needed to reinforce the interconnects or use different interconnects material.

1.3: Conclusion

Overall, the field of stretchable electronics holds great promise for various applications, particularly in wearable devices and biomedical sensors. While there are still several obstacles to overcome, advancements in the integration of SMDs and stretchable substrates have allowed for the creation of stretchable electronic circuits that can conform to deformable interfaces. Future research in this area should focus on addressing the challenges involved in fabricating highly-stretchable wiring, creating robust interconnections, and achieving large-scale manufacturing and fabrication of stretchable electronics. With further developments, stretchable electronics have the potential to revolutionize the field of electronics and improve the performance and comfort of wearable devices and biomedical sensors.

Chapter 2: Design and Fabrication of Stretchable Electronics' Substrate

In this chapter, I will introduce a fast and simple method of fabricating substrates for stretchable circuits using conductive nanostructured gold, referred to as 'wrinkled gold', as the functional material. The wrinkled gold structure ensures easy fabrication and high stretchability up to 130% strain without specific and cautious design. By leveraging the wrinkled gold's nano-microstructure and its tolerance to strain, we are able to design all conductive paths as easy-to-fabricate straight lines instead of serpentine or mesh patterns. Additionally, unlike some partially free-floating[14,25] or liquid metal[21,23] designs, the conductive gold layer is strongly chemically bonded to the PDMS substrate layer, which ensures the robustness and durability of the circuit. All conductive traces are designed and laser etched precisely via laser ablation to ensure time efficiency. Multiple devices may be laser ablated in parallel to save time and achieve large-scale manufacturing capacity. To alleviate the stiffness mismatch issue between SMDs and the conductive layer, a specially designed low-cost nylon mesh reinforcement is sandwiched between SMDs and the conductive layer, and conductive silver epoxy is used.

2.1: Wrinkled Gold Structure

The fabrication process for the wrinkled gold structure involves several steps, including metal deposition, pre-stressing of the polystyrene sheet, shrinking protocol, application of MPTMS, covering with PDMS, curing, and lift-off of the thin gold film. The process is improved from previous protocols reported by Pegan et al. [35] and Zhou et al. [1] by controlling the thickness of the metal layer and optimizing the shrinking protocol.

First, a magnetron sputter is used to deposit a 60 nm layer of gold onto the pre-stressed polystyrene sheet. The sheet is then placed in a convection oven at 140 °C for 13 minutes to allow the PS to flow back to its original shape without stress. During this step, the metal layer buckles under the stress caused by the shrinking of the PS, forming wrinkles.

To ensure the surface smoothness of the sample, a piece of heated glass at 140 °C is placed on top of the sample, and a weight of 1 kg is applied while the sample is still soft under heat. The sample is then allowed to cool down to room temperature.

Next, the sample is placed in a five mM 3-mercaptopropyl trimethoxysilane (MPTMS) ethanol solution for 2 hours. The MPTMS bonds to gold and silicone chemically. After rinsing away excess MPTMS, the dried sample is covered with polydimethylsiloxane (PDMS) and spin-coated at 500 RPM for 30 seconds. The sample is then degassed for 10 minutes in a vacuum chamber at -96 kPa and cured under 60 °C for 1 hour.

The PDMS and the functional gold thin film are lifted off from the polystyrene by submerging the sample in a 60 °C acetone bath for 20 minutes. The PDMS and bonded gold thin film are further cleaned by toluene sonication and rinsed with acetone. Finally, the substrate is dried at room temperature before laser ablation.

The wrinkle structure improves the durability and stretchability of the metal film. When the substrate is strained linearly, deformation of the substrate causes elongation of the thin metal film. In

comparison to planar thin films, the wrinkled film allows for a considerably larger dynamic range because the wrinkles unfold, align to the axis of strain, and stretch before cracks form. The subsequent cracking corresponds to a steeper increase in resistance as the cracks propagate and coalesce. In one of my previous research projects, as shown in figure 1a, platinum wrinkles were observed to stretch along the direction of the applied strain, indicated by the arrow. Cracks were formed as well. The red pseudo-color illustrates the exposed bottom polymer substrate and the cracks around it. The wrinkles act as an additional strain relief, allowing for a considerably larger dynamic range before irreversible failure. Although gold and platinum are different, the general working principles are still the same, and this is the basis of stretchable wires and sensors. Usually, platinum presents more cracks and higher resistance change, and gold is more suitable for conductive wire applications.

2.2: Conductive Wires and Stretchable Strain Sensor on the Stretchable Circuit

All the conductive traces and strain sensors are designed in AutoCAD and etched by laser ablation on the substrates prepared in the previous step. The infrared laser cutter is set at 12% of its maximum power and 70% of its maximum speed, respectively, and 1000 PPI. The high-energy laser beam will penetrate through the surface metal and into the PDMS substrate. The top layer of PDMS is burnt, and the attached metal will come off. After the laser ablation is completed, the substrate is submerged in 70% ethanol and sonicated for 15 seconds to remove any possible debris and dust. The substrate is then dried before mounting SMDs using interconnects.

The strain sensor used to measure respiration is embedded in the stretchable device and has the same thickness as the conductive wires. However, the initial piezoresistive strain sensor in our lab was introduced by Pegan et al. [35]. Later, a super-sensitive strain sensor was introduced by Zhou et al. [1]. Both types of strain sensor utilize platinum as the functional material, as platinum is more brittle and can form micro-cracks easier than gold. Gold, on the other hand, is more conductive and less sensitive to strain change, which makes it ideal for conductive wire material. However, with the integration of the strain sensor into the stretchable circuit board, extra work and time are required to deposit two types of metal onto the same piece of material. As tested by Kim et al.[36], gold wires can work as a strain sensor but with lower sensitivity. Therefore, I decided to use gold as the functional material for the strain sensor as well.

However, the resistance of the gold wire changes regardless of whether it is used as a wire or a strain sensor. To ensure that most of the resistance change comes from the strain sensor, the resistance of the sensor needs to be significantly larger than that of the wire. The width of the conductive wire is 1 mm. In order to increase the local resistance of the strain sensor, the width of the trace is significantly reduced to 0.2 mm, and the length of the trace is elongated significantly compared to the wire. Serpentine design is also applied to increase the sensor density. As a result, the resistance of the sensor

is approximately four kOhm, while the resistance of the wire is approximately 20 Ohm. By deliberately designing the locations of SMDs and sensors, I am ensuring that most of the strain and resistance change is from the sensor area.

2.3: Conclusion

The stretchable substrate and metal conductive layer are created by shrinking low-cost pre-strained PS film. Due to the wrinkle structures on the metal film, the metal film can now be stretched much further compared to the plain structure. To speed up the metal deposition process, we outsource the metal deposition work, and we have a huge roll of PS film with pre-sputtered gold. After the casting and transfer process, the entire sample becomes stretchable. Then laser ablation is used to create the sensors and conductive wires precisely and quickly.

In the next chapter, I will talk about the super-sensitive strain sensor[1] in detail and explain how it works. Furthermore, I want to describe how it facilitated the development of stretchable circuits and devices.

Chapter 3: High-Resolution Integrated Piezoresistive Sensors

In this chapter, I present a completely encapsulated wrinkled metal thin film-based flexible piezoresistive sensor with a tunable elastic modulus that can measure micron-scale strain. Because of its extreme sensitivity, we demonstrated its effectiveness for monitoring microfluidic strain, device pressure, and valve state. This soft strain sensor has a dynamic range of 50% and can detect linear displacements as small as 5 μm (0.025% strain). The displacement of the sensor can be used to calculate the force applied to the sensor. Due to its high strain sensitivity to linear stretching and ultra-soft substrate, small pressures applied on the surface will deform the sensor, causing it to expand orthogonally to serve as a highly sensitive pressure sensor for microfluidic applications. The pressure measured from the microfluidic device can be correlated to the flow rate in the channel as well. Finally, the sensor can be integrated into a pneumatic valve to monitor valve actuation. To the best of our knowledge, there is no such sensor that can electrically monitor valve state in microfluidic devices.

3.1: Background and Motivation

Microfluidic devices used for molecular analysis, cellular analysis, and drug screening require precise control of parameters such as pressure and flow rate[37–42]. To achieve fluid delivery, off-chip hardware, including pressure regulators for pressure-driven flow and syringe pumps for controlling volumetric flow, are commonly used. Although integrated valves can be used for on-chip routing and switching of fluids[43–45], they are still dependent on external pressure sources and solenoids for control. Furthermore, feedback from these systems, such as pressure or flow rate, is typically provided by sensors off-chip, either in the tubing connected to the device or integrated into the perfusion hardware.

Despite the significant advancements in micro total analysis systems in recent years, there is still a lack of widely accessible on-chip monitoring and closed-loop control of fundamental parameters. This lack of on-chip monitoring solutions creates inherent limitations in the responsiveness and accuracy of the measurements that can be obtained. The use of off-chip hydraulic and pneumatic sensors is limited by the dead volume of the interface tubing connecting the sensors to the chip. This dead volume is usually larger than the volume of the microfluidic device, and it can dominate the response time and accuracy of a measurement.

Integrating local measurement options for fundamental parameters into microfluidic systems is currently challenging. While optical sensors can provide precise and reliable flow and pressure measurements, they require coupling to expensive and complex imaging systems[46–49]. Micro electromechanical systems (MEMS)-based sensors offer high-resolution on-chip integration, but their fabrication is typically complex, and contact-based measurements can lead to confounding factors such as fouling. For example, in-channel sensors that extend into the fluid channel can affect the local flow profile and suffer from fouling, which can cause inaccurate results due to increased drag force[50].

Commercially available MEMS sensors are not designed for single-use applications, creating a cost and complexity mismatch that limits their widespread integration[51].

Soft and stretchable sensors have garnered considerable interest in research due to their ability to conform to different surfaces and their wide dynamic range under deformation. These sensors can convert mechanical displacement into electrical signals, such as changes in resistance or capacitance. Among them, liquid metal-based pressure sensors with a PDMS substrate are a popular choice for integration into microfluidic devices. However, channels containing liquid metal require extra precautions during fabrication and are more prone to mechanical failure. Alternatively, thin metal film-based sensors offer attractive performance and robustness characteristics and are easier and safer to fabricate and handle[52–54]. These sensors are able to sense mechanical deformations in various planes, and the resulting electrical signals can be correlated and calibrated to physical parameters-of-interest. However, soft strain gauges have typically been limited to macroscale applications[55–57], and there are few reports of soft sensors capable of monitoring micro-scale strains. Recent papers focused on micron-scale sensors still report monitoring deformations on the millimeter scale[58]. Monitoring deformations from extremely small forces requires unique strategies. For instance, wearable sensors may not respond linearly in this micro regime, and gauge factor has been reported to be different between low strain range and high strain range[35,59]. Moreover, in micro-applications, the system may not be able to actuate the strain sensor due to limited force output. For example, the small force generated from a monolayer of cardiomyocytes or small pressure changes in a microfluidic channel may not be sufficient to drive conventional rigid force gauges. The stress generated by an isolated muscle strip ranges from 8 to 20.7 kPa[60], which is not strong enough to drive conventional rigid force gauges.

To date, there are a limited number of papers that have demonstrated the effective application of flexible sensors in micro-device monitoring[59,61]. Parker and colleagues developed a high-sensitivity piezoresistive sensor using multi-material 3D printing to monitor stress induced by cardiac tissues, with

a reported minimum tested strain of 0.0125%[61]. Flexible sensors such as this have the potential to replace traditional optical methods to monitor tissue contractility[62]. Wen and colleagues developed a silver powder doped-PDMS-based piezoresistive pressure sensor that can be bonded to a microfluidic device[59]. When the pressure in the channel increases, the flexible sensor is stretched.

In situations of pressure-driven flow, the pressure is directly proportional to the flow rate. Thus, the flow rate can be calculated from the pressure measured by a sensor in the fluid channel. While most report noncontact flow meters to have a resolution of tens to hundreds of µl/min[63–65], some research groups have demonstrated nanoliter resolution temperature flow sensors[66] and 0.5 µl/min resolution microwave flow sensors[67]. However, temperature flow sensors[66] could be disturbed by non-flow effects, such as environmental heat flux flowing into sensors during experiments. Unlike other parameters, pressure is still a flow indicator that is independent of surrounding noise, such as electromagnetic waves and heat flux. In the flow sensor by Sanati-Nezhad and colleagues, pressure in a microfluidic channel deforms a membrane to modulate the permittivity of a microwave resonator, thus producing a flow measurement[67].

From the current literature on available sensors for micron-scale in-situ monitoring, there remains a need to develop a universal sensor compatible with soft lithography that can be scaled, arrayed, and used to measure a range of critical microfluidic parameters.

3.2: Method

3.2.1: Sensor Fabrication

Fabrication of the soft strain sensors was improved for sensitivity from the previous protocol reported by Pegan et al. [35]. Specifically, we tuned the thickness of the metals, improved the shrinking protocol, developed a soft, customized PDMS substrate, and introduced an encapsulation layer on the sensors. Briefly, a layer of single-sided adhesive plastic shadow mask film is applied to a pre-stressed polystyrene sheet. The geometry of the mask is designed by laser etching and then lifted off from the polystyrene sheet. Then a thickness-controlled magnetron sputter deposits 40 nm of Pt and 5 nm of Au onto the masked polystyrene sheet. The mask is removed, and the polystyrene sheet is put in a convection oven set at 140 degree Celsius for 13 minutes. After the sheet shrinks under heat, the sample is placed in a 5mM 3-mercaptopropyl trimethoxysilane (MPTMS) ethanol solution for 2 hours. After rinsing away the excess MPTMS, the dried sample is covered with polydimethylsiloxane (PDMS), which has a mass ratio of 1:20:4.2 cure to base to dimethyl silicone fluid (PMX 200), and spin-coated at 800 RPM for 35 seconds. The sample is placed in the vacuum to degas and is then cured at 60°C overnight. The PDMS and the functional metal thin film are lifted off from the polystyrene by submerging the sample in a heated acetone bath. The PDMS and bonded thin metal film are further cleaned by additional acetone and toluene rinsing. In order to make the metal film electrically isolated from the environment, another layer of PDMS with the same composition as above is spun on the other side at 1000 RPM for 35 seconds. The sample is placed at room temperature for at least 48 hours to cure. After curing, the final sensor geometry is designed, and laser etched through. The pad area of the sensor is sandwiched by two pieces of acrylic to reduce any potential movement to the pad and connection area. The 28-gauge silicone wires are connected to the pad with silver conductive epoxy (M.G. Chemical Ltd).

3.2.2: 5 µm Resolution Benchtop Setup

A Zaber linear actuator (Zaber Technologies Inc) is mounted onto a custom acrylic stage, and the entire system is placed within a custom acrylic box to prevent any possible environmental air flow that might affect the signal acquisition. The stage contains two parts: one part is stationary; the other part is able to slide on a track uniaxially. The driving side of the linear actuator is connected to the moving part of the stage. The pad side of the sensor is mounted on the stationary side of the stage, while the other side of the sensor is clamped onto the moving portion of the stage. A Precision LCR Meter (Keysight Technologies E4980AL) is used to acquire resistance data of the sensor. A Labview-based program is used to control the movement of the stage and collect stage position data from the linear actuator and sensor resistance data from the LCR meter. The linear actuator applies 6 consecutive groups of micro-cycles of 5 µm, and each group contains 300 cycles. Then the entire process is repeated at different frequencies.

3.2.3: Pressure Sensitivity Test

A 3mm x 15mm x 1.5mm (w x l x h) acrylic piece is placed over the sensor trace area directly, and a metal probe is attached to a force gauge (Mark 10 M5-025). The force gauge is mounted on the test stand (Mark 10 ESM 303) and moves down at 20 µm/s speed until it comes in contact with the acrylic piece. The test is repeated 5 times.

3.2.4: Channel and Device Dimension and Assembly

The microfluidic device contains two parts: a channel and a sensor. The channel is made with positive mold on a piece of PDMS (Young's modulus ~2.6Mpa[68]) and has a cross-sectional dimension of 50 µm x 150 µm. The total length of the channel is 241.7 mm. For flow rates from 1 µl/min to 200 µl/min, the Reynolds number remains smaller than 40. Thus, the working range is always stable laminar flow, and there is no noise due to turbulence.

The thin film-based piezoresistive sensor consists of two layers of PDMS with customized

stiffness (Young's modulus ~250Kpa) and one layer of wrinkled bimetallic thin film (platinum and gold). The total thickness of the layer is ~100 μm. The metal film is sandwiched and firmly bonded between PDMS layers to stay insulated and prevent wearing and scratching. The polymer layers and wrinkled metal film will deform under stretching or compression; due to the brittle wrinkled structure of the metal film, micro-cracks will form. As more and larger cracks form on the metal film, the electrical resistance increases.

The sensor is directly embedded at the bottom of the chip and serves as the base of the channel. The pressure required to drive fluid flow deforms the channel. As the upper and side walls of the channel are about 10-fold stiffer than the bottom sensor wall, most of the deformation will occur on the sensor surface. The electrical resistance of the sensor increases due to the deformation described above.

3.2.5: Microfluidic device fabrication

The microfluidic device comprises two parts: a sensor and a channel. The sensor part follows the same procedure as regular sensor fabrication until the curing of the encapsulation layer. After curing, the sensor is ready for plasma treatment. The channel device is fabricated through a traditional replica molding process (a detailed flow chart is shown in supplemental Figure s6). The positive mold is created by applying a layer of single-sided adhesive plastic film (Frisket Film from Grafix Art) on a piece of acrylic base. The shape of the channel is designed by laser etching the outline of the channel geometry. Excess plastic film outside the channel geometry is removed after laser etching. An acrylic well is adhered to the base to create a mold. 10:1 base-to-cure ratio of PDMS is poured into the mold, degassed for 20 minutes, and cured for 2 hours under 60 °C. The PDMS channel device is removed from the positive mold, and a biopsy punch is used to create an inlet and outlet. After cleaning both device and the sensor with tape, the bottom side of the sensor and the channel side of the device are placed in the plasma machine (Plasma Etch) and treated for 3 minutes. Then the sensor and device are placed with treated

sides against each other and cured at 60 °C for over 2 hours for stronger bonding.

3.2.6: Microfluidic flow rate measurement

The outlet of the microfluidic chip is connected to a plastic pipeline and open to the air. The inlet of the microfluidic chip is connected to a 3 ml syringe and controlled by a syringe pump. The syringe pump is programmed to deliver a specific flow rate to perform relevant working range, resolution, accuracy, repeatability, and leak tests. An inline pressure transducer (Omega PX 409) is connected to the syringe outlet via a T-shaped connector. A Precision LCR Meter (Keysight Technologies) is used to acquire sensor resistance data.

3.2.7: Valve integration

Microfluidic valves and digital logic circuits were fabricated similarly to previous works[45]. Microfluidic channels were machined into sheets of PMMA (Polymethyl methacrylate) using a CO_2 laser (VLS 2.3, Universal Laser Systems), and devices were assembled by aligning and sandwiching the channel layers (channel has a width of 400 µm and depth of 400 µm, a resistor has a width of 200 µm and depth of 200 µm) around a piece of sensor-embedded PDMS (~600 µm thickness). The sensor was situated directly over the valve. For the flow control valve, a constant vacuum pressure of -85 kPa was applied to one side of the flow layer while a mass air flow meter (Zephyr HAF, Honeywell) was connected to the other side through 150 cm of 0.02" ID Tygon microbore tubing. The valve was switched on and off with a period of 10 s and a control pressure of -85 kPa delivered via a computer-controlled miniature solenoid valve (S10, Pneumadyne, Plymouth, MN) while air flow measurements were acquired at a frequency of 90 Hz. Inverter gates were constructed similarly, leaving the input to the inverter open to room air and adding a pressure sensor (PX139, Omega) to the output of the gate. Pressure measurements were acquired at a frequency of 50 Hz. The oscillator pump consisted of a ring oscillator formed from three

identical inverter gates connected in a ring and three liquid handling valves, each connected to the output of an inverter. The flow rate of air from the peristaltic pump was measured by a hot wire anemometer (Zephyr HAF, Honeywell) connected to the output of the pump, while images of the incident light reflected from a pump valve were acquired at 240 Hz by a camera (iPhone Xr, Apple Computer). The average pixel intensity of a region of interest over the valve was extracted and processed with a custom program written using OpenCV[69].

3.3: Results and Discussion

3.3.1: Characterization of Sensor Performance

We first characterized our piezoresistive sensors with integrated nano-to-micro scale wrinkled structures (Figure 1). This thin film is supported on and encapsulated with a silicone elastomer. The resistance change of the sensors is based on crack formation within the wrinkled film when stretched. When the sensor is strained linearly, deformation of the substrate causes elongation of the thin metal film. In comparison to planar thin films, the wrinkled film allows for a considerably larger dynamic range because the wrinkles unfold, align to the axis of strain, and stretch before cracks form. The subsequent cracking corresponds to a steeper increase in resistance as the cracks propagate and coalesce. In Figure 1a, wrinkles were observed to stretch along the direction of the applied strain, indicated by the arrow. Cracks were formed as well. The red pseudo-color illustrates the exposed bottom polymer substrate and the cracks around it. The wrinkles act as an additional strain relief, allowing for a considerably larger dynamic range while maintaining high sensitivity before irreversible failure.

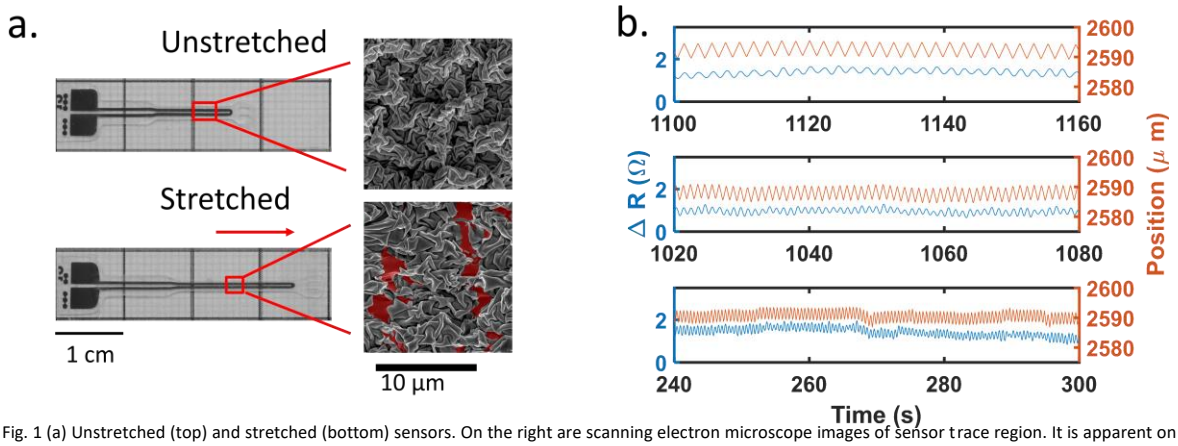

Fig. 1 (a) Unstretched (top) and stretched (bottom) sensors. On the right are scanning electron microscope images of sensor trace region. It is apparent on the SEM that the wrinkles align and stress in the direction of actuation. Fractures in the thin film have been illustrated by pseudo-coloring the exposed polymer layer in red. (b) Sensor's resistance response under different cyclic frequencies (from top to bottom are 0.5, 1, and 2 Hz respectively). The sensor (blue) tracks the displacement of 5 µm (red) very well, and the baseline shift is captured for 2 Hz as well (~265 s). 5 µm corresponds to 0.025% strain of the sensor.

The composition of the functional metal thin film was tuned to achieve a balance of brittleness

and stability in the sensor to achieve a stretch resolution of 5 microns. The thin metal film is a bilayer of platinum and gold. Material brittleness will affect the number and size of cracks that form, along with the energy required to form cracks. Platinum is a more brittle material, while gold has good ductility[70]. A thicker platinum layer results in more and larger cracks but leads to unstable resistance. As a more ductile material, a gold layer will lead to fewer cracks, but the change in resistance is significantly smaller. A balance can be achieved by controlling the thickness of platinum and gold, respectively. After testing various combinations, we chose a 40 nm platinum along with a 5 nm gold layer because it provided the highest signal detection while still maintaining stability. The sensor's substrate is 70 µm thick PDMS, with an encapsulation layer of 30 µm PDMS, with the wrinkled metal layer sandwiched in between the PDMS layers. A detailed cross-sectional dimension of the sensor is shown in supplemental figure s1.

To calculate the conversion between mechanical displacement and corresponding force, certain approximations and assumptions were made. As the sensor is stretched at the micron scale with negligible deformation, the deformation of the sensor is assumed to be a uniform beam that is undergoing uniaxial stress and has elastic-like behavior. From equation 1:

$$\sigma = E \cdot \varepsilon \tag{1}$$

where σ is stress, E is Young's Modulus, and ε is strain

We can further expand on this in equation 2:

$$\frac{F}{w \cdot h} = E \cdot \frac{\Delta L}{L_0} \tag{2}$$

where F is the uniaxial force, w and h are width and thickness of cross-sectional area, ΔL is the change in length, and L_0 is the original length. Thus, to reduce the force required to actuate the sensor to displace 5 µm, the elastic modulus of the silicone substrate was lowered to 250kPa by adding dimethyl silicone fluid (PMX 200) to a mixture of a 20: 1 base-to-cure mass ratio Polydimethylsiloxane (PDMS), and substrate dimensions were adjusted to 20mm X 2mm X 0.1mm (l X w X h). The combination of these

constituents allows the sensor to detect as low as 20 μN uniaxial force, which corresponds to 5 μm linear displacement.

Figure 1b shows a representative sensor's behavior under different stretching frequencies. It demonstrates the sensor's repeatability. The sensor's pad area is fixed on a linear actuator (Zaber Technologies Inc), with the tip area clamped on a moving stage. The moving stage was cycled by 5μm at 0.5, 1, and 2 Hz, respectively, while the sensor tracked the changes accordingly. A baseline shift of the stage movement was also captured at ~265s for 2 Hz. While it is not obvious in the figure, there is a signal delay between the position and resistance. For 0.5, 1, and 2 Hz, the response times are 169, 80, and 27 ms, respectively.

To further understand the signal latency, one more experiment was performed. As shown in Figure s2a, a typical sensor was stretched by 200 μm at a speed of 200 μm/s, held for 10 seconds, and released back by 200 μm at a speed of 200 μm/s. The position of the linear actuator and the resistance of the sensor were both recorded. 34 tests (N=10 sensors) were performed. On average, the actuator began to move at 5.03±0.01 s while the sensor began to detect a resistance change at 5.08±0.08 s. The stop time was defined as the time at which the sensor or actuator reached 90% of the value of the maximum relative change. The actuator stopped at 5.90±0.02 s, and the sensor stopped at 5.95±0.1 s. The data indicates that the sensors have an average response time of 50 ms. Computer processing and device communication time, however, also contribute to this response time.

To observe signal hysteresis, the sensor was cycled to 150 μm and stretched at 20 μm/s speed 20 times. The hysteresis for a representative sensor is shown in supplemental figure s2b. From this figure, although reproducible, the sensor's resistance followed different trajectories when stretched and released at large deformations. With the loading and unloading behavior displaying different sensitivities, it is important to know which trajectory the sensor is on when tested. Supplemental figure s2c shows a representative sensitivity curve in terms of the change in resistance versus the change in

length. As the sensors were initially stretched, wrinkles in the thin metallic film unfolded, resulting in minimal changes in resistance. As strain increases and cracks form and propagate, the resistance increases nonlinearly.

3.3.2: Calculating Flow and Pressure

The sensor was integrated with the microfluidic chip by plasma bonding the microfluidic chip directly onto the sensor. The sensor had the same structure and design as the one used for stress-strain testing, except the PDMS substrate was larger and had not been cut into a dog bone shape.

When fluid is pushed through the microfluidic device, the pressure within the channel deforms the membrane of the piezoresistive sensor (supplemental figure s3) and changes the electrical resistance of the functional metal film. As shown in Figure 2a, the channel (clear, blue) overlaps with the sensing area (black).

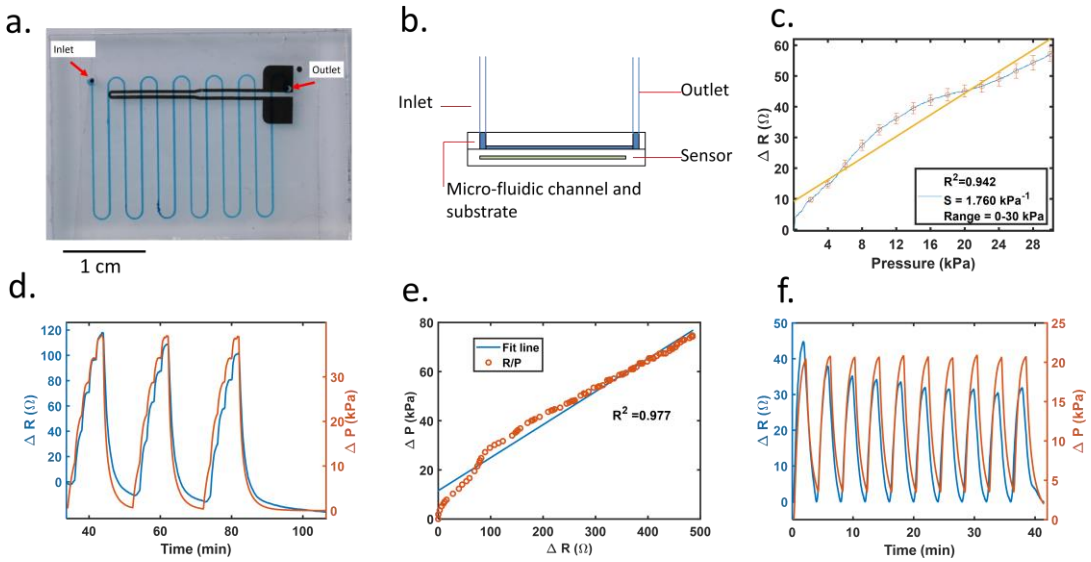

Fig. 2 (a) Picture of a microfluidic device with embedded sensor. (b) Schematic cross-section of device. (c) Pressure sensitivity or the sensor, the sensor is compressed 5 times. Blue line is the actual sensor sensitivity curve with red bars as standard error at each 2 kPa increments, and the yellow line is the linear fitting line. A R^2 value of 0.942 is achieved. (d) Pressure and sensor data for flow rate increases from 0 to 50 µl/min in 10-µl/min increments, and repeated 3 times. (e) Change of pressure vs. change of resistance as flow rate increases from 0 to 200 µl/min. (f) Post-processed sensor resistance and pressure tracings for 10 cycles of flow rate from 0 to 20 µl/min. The processed sensor signal decay stabilizes after 3 cycles.

When pressure is applied normal to the sensor surface, the sensor substrate will expand in the transverse plane. Lateral expansion of the sensor elongates the metal film causing cracks to appear; when pressure is reduced from the surface, the substrate returns to its original shape, and the fractured

metal will come back into contact with each other. Due to the design difference between the trace and pad area, the pad area had a larger metal area. However, from the simulation results in Figure s4, the pressure within the region that overlaps the sensor pad area was several folds smaller than that of the region overlapping the trace area.

We assessed several aspects of the sensor performance, including working range, resolution, accuracy, and repeatability. For our microfluidic device, with a working flow rate range of 6 µl/min to 200 µl/min, the measured pressure from the inline pressure sensor of the inlet fluid varied between 1 kPa to 74 kPa. Figure s4 depicts a simulation of pressure within the channel under a 10 µl/min flow rate. The pressure map shows the gauge pressure, which can be related to deformation on the channel wall and sensor. Gauge pressure inside the channel drops along the pathway and reaches 0 at the open-air outlet indicated in Figure 2b. With a channel width of 250 µm and a trace width of the sensor of 300 µm, the overlap area is small in comparison to the entire sensor. The deformation of a single overlap area may be too small for the signal change of the sensor to be detected. Thus, multiple sensor-channel crosses are used to increase the overlap area to boost the signal. However, from the simulation (figure s4), the pressure drops along with channel length, and the deformation of the cross area will become smaller with less pressure. As a result, more overlap will increase the total signal sensitivity but with diminishing returns. With the variable pressure along the channel and the sensor having multiple crosses within the channel to increase signal change, it is difficult to detect localized pressure. In this configuration, the sensor detects overall deformation caused by the pressure.

To confirm our results, a pressure sensitivity test was performed on the sensor. A 3mm by 15mm acrylic flat was placed over the sensor trace area. A force gauge (Mark 10 M5-025) was fixed on a test stand (Mark 10 ESM 303) and placed into contact until pressure was applied to the acrylic piece. As the pressure increased, the sensor's resistance increased as well (Figure 2c). The blue line is the average resistance across 5 runs. Red markers indicate the standard error at every 2 kPa increment. The yellow

line is the linearly fitted line, which has an R^2 value of 0.942. From the graph, although the resistance value varies across sensors, they all follow the same trend and are relatively linear, especially at low pressures.

Figure 2d represents a variable flow rate test showing pressure and sensor data versus time. The flow rate increases from 0 to 50 µl/min in 10 µl/min increments, and the entire test is repeated three times consecutively.

The working range for our device is 6 µl/min to 200 µl/min. The criterium for minimum resolution is that the signal change between two different flow rates is at least 3-fold larger than the root mean squared noise. In a flow rate test ranging from 0 to 30 µl/min with 2 µl/min increment, data shows that the minimum detectable flow rate is 6 µl/min, and the resolution is 2 µl/min (figure s5). Although the flow rate working range for our device is tested to an upper limit of 200 µl/min (as shown in Figure 2e), the device has been tested up to 300 µl/min without failure (data not shown).

Although sensor data shows a good correlation to changes in pressure and flow rate, the baseline signal decays when strain is removed, and the sensor returns to an unstretched state (as shown in Figure 1c). The flow rate drops from 20 µl/min to 0 µl/min, as shown in Figure 2f. Signal decay is noticeable when the sensor reading drops, even when the linear actuator or syringe pump is idle. The decaying tails observed in Figure 2d and supplemental Figure s2a illustrate the baseline decay with a time length greater than ~85 min. Similarly, signals at zero flow rate decrease in value as well (Figure 2d, four separate zero flow rate points are ~35 min, 55 min, 75 min, and 90 min). This decay complicates the data analysis and limits the duration that the resistance to pressure relationship is accurate but can be accounted for with subsequent data processing. Because baseline decay occurs in all sensor data, every test data has a different baseline value. In order to compare inter-trial data with different starting baselines, all data are subtracted by the beginning baseline resistance so that it starts at 0. Additionally, the decaying trend is compensated by data post-processing. As shown in Figure 2f, the value of each

valley was extracted and set to 0 ohms. Each valley point is used to form a linear interpolated line. The data points between the valleys were adjusted by subtracting the linearly interpolated lines, between the valley, from the signal so that the sensor signal at each zero flow rate is set to 0 Ohm.

System elasticity is one minor issue that contributes to signal decay; another possible contribution to signal decay is polymer relaxation. Relaxation is an intrinsic property of the polymer substrate. As the channel wall and sensor floor undergo mechanical hysteresis and relaxation, the formation and contact points of cracks in the embedded thin metal film are affected, resulting in electrical hysteresis as well. Other groups demonstrated that the hysteresis in piezo-resistive-based elastomeric strain sensors could be potentially accounted for using machine learning [71].

To ensure the repeatability of the sensor, conditioning tests were performed on the chip device. The fluid flows through the pre-primed device at 20 µl/min for 2 minutes and then pauses for 2 minutes; this cycle is repeated 10 times. The sensor resistance difference between 0 and 20 µl/min is compared for 10 cycles (Figure 2f). Although some decay remains, the difference in resistance decrease is greatly reduced after 3 cycles.

3.3.3: Valve Sensor

The microfluidic valves used in this study were normally closed elastomeric membrane valves similar to those first reported by the Mathies group [44]. A valve consists of two layers of microfluidic channels sandwiched around a thin elastomeric membrane. The valve is opened by applying a vacuum to the control layer, deflecting the membrane, and connecting the channels on the opposite side. The piezoresistive sensor was embedded in the elastomeric membrane with the sensing element placed directly over the seat of the valve, allowing the sensor to detect the valve opening or closing when the

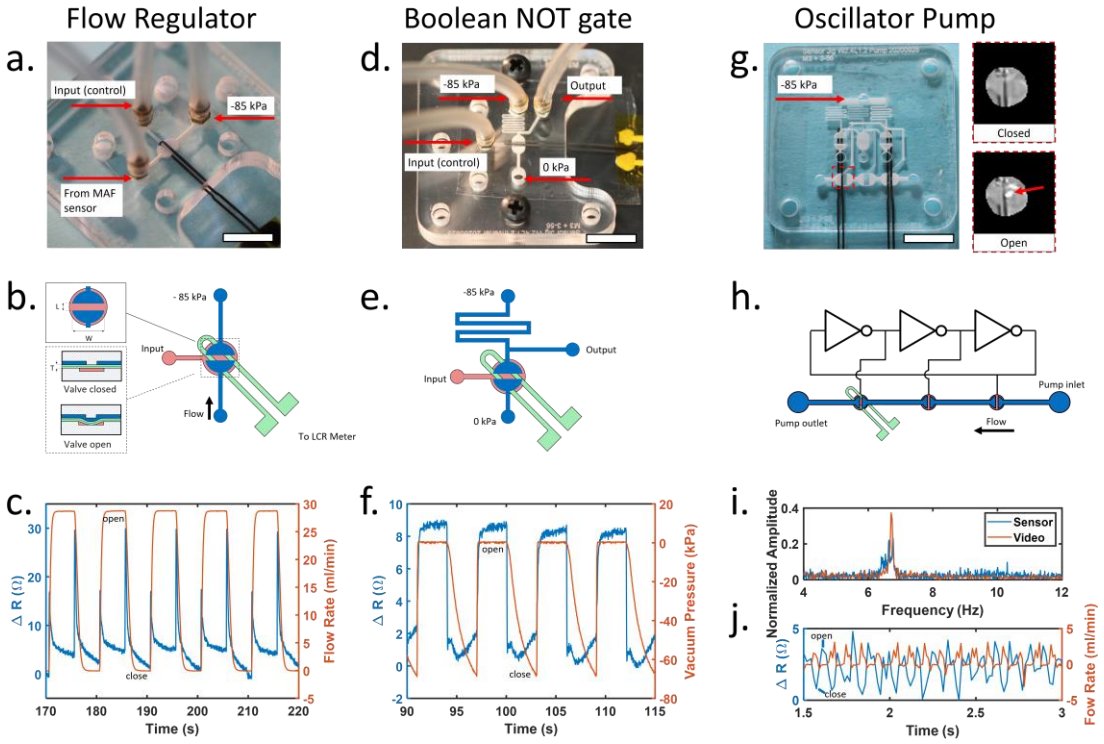

Fig.3 (a) Sensor integrated into an elastomeric membrane valve for control of reagent flow. White scale bar is 1 cm (b) Valve construction details. Close up view of overhead (top inset) and cross-section of valve (bottom inset). Channels on the control and flow layers are shown in red and blue, respectively. Sensor is embedded in the membrane shown in green. Valve seat length (L) = 1.2 mm, valve seat width (W) = 2.4 mm, membrane thickness (T) = 0.6 mm. (c) Sensor resistance increases when the valve is opened or closed. (d) Sensor integrated into a microfluidic inverter logic gate for microfluidic computing. (e) Inverter gate construction details. Channels on the control and flow layers are shown in red and blue, respectively. Sensor placement shown in green. (f) Comparison of sensor resistance and inverter output over time. (g) Photo of microfluidic oscillator pump with integrated sensor. Light reflected from a single valve was used for high speed video analysis (inset). Only the sensor on the left is used. (h) Schematic of peristaltic pump controlled by integrated ring oscillator circuit. The sensor was placed under the final pump valve to detect opening and closing. (i) A comparison of sensor data and high-speed video for monitoring oscillation frequency show matching peaks at 6.71 Hz. (j) Flow rate from the peristaltic pump measured using external hot wire anemometer and corresponding sensor measurements from the final valve in the pump. All scale bars are 1cm.

sensor was stretched or relaxed.

We first investigated the ability of the integrated piezoresistive sensor to measure the state of a valve configured to switch fluid flow on or off (Figure 3a). An external hot wire anemometer (Zephyr HAF, Honeywell) was configured to measure the flow rate of air through the valve as it was opened and closed. Upon valve actuation, the integrated sensor produced a sharp spike in signal followed by an increase in baseline resistance when opened and a decrease when closed. These results show the membrane stretching before the valve opens, followed by the membrane remaining in a partially stretched state while the valve remains open (Figure 3c). Upon closing, the sensor signal spikes again as the vacuum is released, and the membrane contacts the valve seat sealing the valve closed. We

observed that the spike that occurred during valve state changes was dependent on the orientation of the sensor and was most pronounced when the sensor was placed directly over the seat of the valve. Data from the external air flow sensor showed the valve completely opened and closed, and the sensor did not interfere with the normal operation of the valve. These results indicate the piezoresistive sensor is suitable for monitoring the state change of the valve.

Normally closed elastomeric membrane valves can also be used to create digital logic gates that are well suited for building integrated microfluidic control circuitry[45]. Therefore, we next investigated the ability of the integrated piezoresistive sensor to measure the state of a valve configured as a microfluidic inverter gate. This circuit adds a pull-up resistor before the vacuum connection to the valve and an output connection upstream of the resistor to produce a digital pressure output signal that is the inverse of the input signal. The sensor reported an increase in resistance of approximately 6 ohms when the valve was opened and returned to baseline when the valve was closed, providing a clear electronic signal that corresponded to changes in the pneumatic output of the inverter gate.

Finally, to create a simple integrated microfluidic control circuit, an oscillator pump[45] was constructed consisting of three identical inverter gates connected in a ring and three liquid handling valves, each connected to the output of an inverter gate (Figure 3g). When a constant vacuum pressure was applied to the oscillator, the pressure sequence generated by each inverter opened and closed the pump valves to create a peristaltic pumping action. The piezoresistive sensor was placed under the final valve in the pump while high speed video imaging was used to monitor the incident light reflected when the valve membrane was pulled open (Figure 3g inset). The oscillation frequency measured by the sensor agreed well with the measurements acquired using high speed video imaging, and the sensor was able to accurately measure oscillation frequencies as high as 24.9 Hz, approximately the Nyquist frequency of our acquisition device (figure 3i and supplementary figure s8). Previous work has shown that the frequency of a ring oscillator can be tuned by changing the input pressure[45] and the average

flow rate of an oscillator pump is dependent on the frequency [72]. Using this information, the oscillation frequency can be used to calculate the average flow rate from the pump.

When placed under the final valve in the peristaltic pump (figure 3h), the sensor readings also aligned well with the pulsatile flow rate measurements acquired from a hot wire anemometer (Zephyr HAF, Honeywell) connected to the output of the pump (figure 3j). A small backflow was detected when the final pump valve opened, which was mostly negated by the closing of the middle valve in the pump. Finally, a strong forward pulse occurred when the final valve closed. Monitoring the state of the final valve in the pump, the sensor can be used to indicate the instantaneous flow rate produced by the pump. A detailed explanation of the working principle of the oscillator is provided in supplementary figure s7.

3.4: Conclusion

We developed a soft, highly sensitive strain sensor that is able to capture 5 µm linear displacement (0.025% strain for 20mm sensor length) in the normal and uniaxial direction and can be deformed with as little as 20 µN of force (100 Pa stress). The response time of our sensor for linear stretching is ~50 ms. In comparison to other flexible pressure and strain sensors' response times, which ranges from ~17 ms to ~100ms[52,73–75], our sensor shows a relatively fast response.

As an indirect flow meter, our sensor also can detect on-site flow rate in-situ as low as 6 µl/min with a resolution of 2 µl/min in our device. However, for our current set up (with only a single sensor), failure will occur if the device is clogged. This causes the pressure to build up and the sensor readings to increase, but nothing will be flowing. In future work, multiple sensors can be used such that separate measurements at each intersection of the channel can be acquired. This allows for more precise local pressure and flow monitoring. Moreover, it will allow for the detection of clogging in the channel. As the pressure increases prior to the clogged point and decreases after the clogged point, the sensors will show relatively high or low readings at different intersections.

For monitoring the microfluidic valve state, our integrated sensor provides a more direct method to monitor valve actuation than existing optical monitoring methods. Currently, the sensor can monitor the binary status of a single valve precisely. Due to the analog output of the sensor, it could potentially detect partially opened valves rather than binary open and closed status; however, this may require individual calibration of each sensor.

The sensor still has some drawbacks. As mentioned in the results section, hysteresis and decay of the signal affect the repeatability of the sensor. With hysteresis present in our system, only the loading signal path is used for analysis. For our strain and liquid flow tests and experiments, we focused on the loading trajectory rather than the unloading trajectory for consistency, particularly as the decay is less severe. For the valve experiment, we are qualitatively checking for the opening and closing of the

valve along with other features of the actuation (such as spikes shown in figure 3). Although hysteresis still exists, it is not critical here and can be compensated for with machine learning algorithms [71] aspects for this specific application.

Due to decay, the signal baseline varies during experiments, so the starting resistance must be subtracted to zero from the baseline for different experiments. Several attempts have been made to minimize hysteresis and decay. In one case, we observed that stiffer substrates demonstrate less decay; however, stiffer substrates require larger loads to deform, which may decrease the detection resolution of the sensor. For some physiological applications, it is impossible to apply larger forces. Thus, adjusting stiffness according to different applications is a potential solution to minimize hysteresis and decay. Additionally, the use of other substrate materials with less intrinsic hysteresis than PDMS is possible, too.

We demonstrated the ability to integrate our soft and extremely sensitive strain sensor into microfluidic devices to provide contactless detection of pressure and correlation with flow rate. The sensor can also be embedded into PDMS-based valves to detect the extent of valve opening in microfluidic devices. Moreover, being PDMS-based, the sensor can be easily trimmed and bonded to any other silicone-based device via plasma treatment. The measurement results show a good linear correlation between sensor reading and flow rate and pressure in the device. The sensor has a flow rate detection range from 6 microliters per minute (μL/min) to 200 μL/min and a resolution of 2 μL/min. The sensor can confirm partial or complete valve actuation under different pressures.

Because the sensor is made of PDMS, it is compatible with soft lithography and easily integrated into microfluidic chips. The stiffness of the substrate, along with the sensitivity and dimensions of the sensor, can be adapted to different applications. The soft and flexible substrate also makes it possible to integrate the sensor into biological applications and monitor micron-scale tissue movement. The sensors can also be readily arrayed; for example, they can be extended from one valve to multiple valves to

measure several valves' status, which is important for large-scale microfluidic systems that require real-time feedback to control each valve.

3.5: Next Step Improvement

The strain sensor is a fundamental building block of stretchable wearable devices and stretchable circuit boards. By changing functional materials from platinum to gold, the sensor will show less resistance change and make it ideal for a circuit board application. The stiffness of the PDMS substrate is also tunable and can be adjusted to accommodate different situations. Another working concept for the strain sensor is the same as the stretchable circuit board. One crucial difference and challenge I need to overcome is the bonding interconnects between stiff SMDs and stretchable substrates, which I will discuss in detail in the next chapter.

Chapter 4: Surface Mount Devices and Integration Method with Stretchable Circuit

In the previous chapter, I talked about how to fabricate a super-sensitive strain sensor and demonstrated it could be used for wearable devices and microfluidics. The next step for potential improvement for the sensor is the acquisition and stiff components. Although the sensor is super sensitive and stretchable, it still requires a separate piece of acquisition device and battery packs to acquire and transmit the signal. It will be a huge improvement if all the components are combined as one. In this chapter, I will talk about how to integrate all the components together into one piece, including the SMDs, Bluetooth acquisition chip, conductive wires, and laser-ablated circuit substrate mentioned in previous chapters. As mentioned before, although there are fully stretchable electronic components, they are still immature and have limited functionalities. As a result, the integration of traditional SMDs and the stretchable substrate is an ideal way to create stretchable circuit boards with multiple functions.

Briefly speaking, the interconnects have a structure that is similar to a composite material. We add a layer of laser-cut nylon mesh in between the SMDs and substrate as the stress relief layer, and conductive silver epoxy is used to electrically bond SMDs and substrate together, which is similar to reinforcement material. A PDMS encapsulation layer is used to form the matrix for the interconnects. This composite-like structure increases the robustness of the interconnects. The high-level idea is the mesh increases the contacting area between SMDs and substrate; the mesh's stiffness is in between the substrate and SMDs. Both factors help decrease the stress and local strain around the actual conductive epoxy contacting points.

We demonstrate that the composite interconnects increase the failure strain of the stretchable circuit board by a significant amount with a simple resistor design and LED array design. We further demonstrate the functionality with the implementation of human respiration monitor board and human ECG circuit board.

4.1: Background and Motivation

There is a significant stiffness mismatch between soft PDMS elastomers and stiff SMDs, such as resistors and capacitors. Compared to PDMS, the stretchability of SMDs is negligible. Without proper processing and assembling, when the circuit is stretched, the PDMS substrate will experience high strain, while the SMD will not. However, the SMD and the substrate are physically and chemically bonded together by conductive epoxy, and there is no strain on the substrate within this interconnects' region. As a result, the substrate around the interconnects will experience a high strain difference when stretched. The high local stress difference will cause fracture on the interconnects and affect the circuit performance, eventually lead to circuit failure.

4.2: Mesh Design and Validation

In order to delocalize the local strain and reduce the sudden change of strain around the interconnects area, an energy-dissipating layer could be utilized to increase interfacial toughness. The energy dissipating layer also functioned to decrease the stiffness mismatch between SMDs and PDMS substrate. A novel composite structure energy dissipating layer was introduced. As shown in Figure 4a, a piece of specially designed laser-cut nylon mesh (SEFAR NITEX) was sandwiched between SMD and substrate as reinforcement material. Silver epoxy was used to connect SMD electrically and mechanically to the conductive layer through the two holes on the mesh indicated in red dash lines. A PDMS encapsulation layer was added on top as the matrix of composite material. The PDMS encapsulation layer filled up the micro-gaps among the mesh and among layers under vacuum and bonded all layers and components firmly after curing.

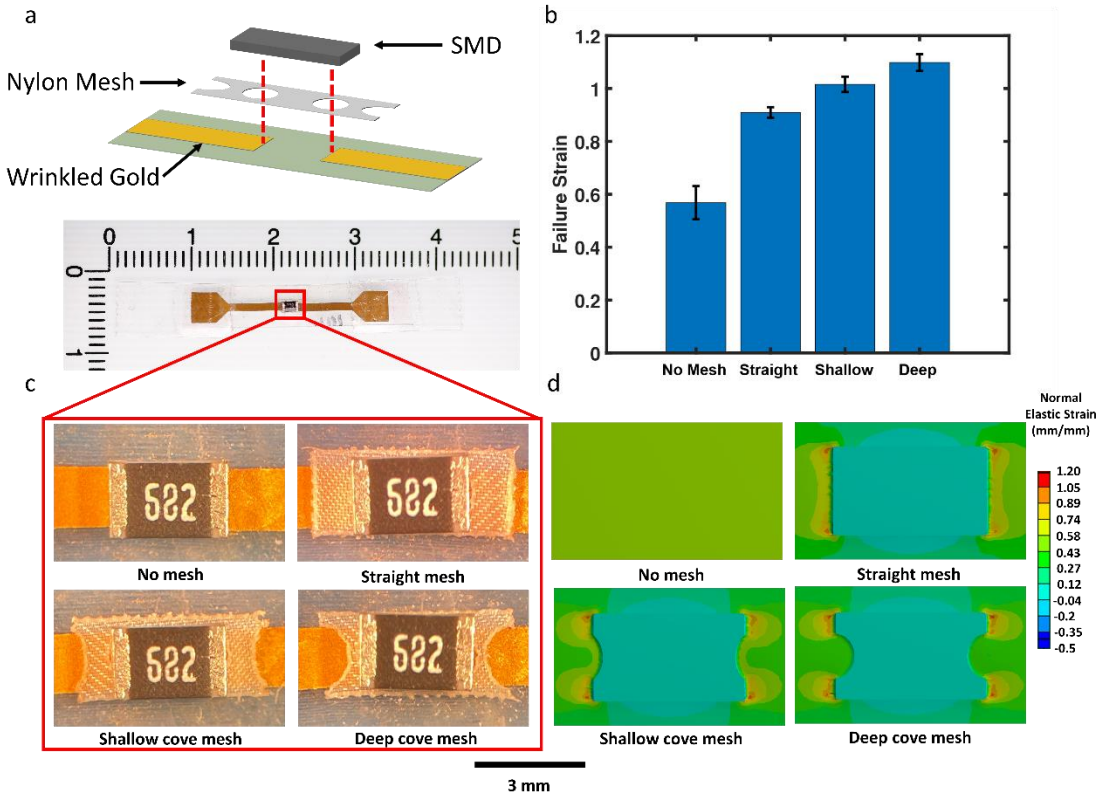

Fig.4(a) Schematic of interconnect structure. b) Results for failure strain test of 4 groups. (c) images of 4 groups of interconnects. (d) Finite element analysis simulation of local strain for 4 types of interconnects.

The mesh and the encapsulation layer together worked as an energy dissipation layer. Firstly, due to the hollow design, the stretchability of the nylon mesh was in between of substrate and SMD, which reduced the significant stiffness mismatch between the substrate and SMD. Secondly, the strain difference at the silver epoxy connection point was smaller when mesh was presented. When mesh was not used, the strain in the PDMS substrate was high, but the strain at the epoxy connection point was near zero; when mesh was used, the mesh had a much lower strain than the PDMS substrate, and the strain difference was smaller. Thirdly, the localized strain near the epoxy connection point was delocalized to a larger area. Originally, the high local strain difference interface was around the epoxy connection points. With the mesh, the stiffness mismatch between mesh and substrate is much larger than it is between mesh and SMD. Thus, the high local strain difference interface was delocalized from the small connection points to a larger mesh area.

Additionally, the geometry, especially the depths and curvature of the cove design on the side of the mesh, was important to the robustness of the interconnects. To find and validate the mesh design, a mesh comparison experiment on resistor design was conducted. The comparison group contains 5 samples whose resistor was bonded to the substrate directly with silver epoxy. The rest three groups contained 5 straight, 4 shallow cove, and 5 deep cove mesh reinforcement designs (figure 4c). A tensile test was performed on each sample until it reached failure strain. The failure strain was defined as the strain at which the circuit became non-conductive or substrate rip. As shown in figure 4b, failure strains of all three groups with mesh (90.9%, 101.5%, 109.8%) were significantly higher than the control group (56.8%), which did not have any types of reinforcement structures. The comparison also showed that the deep cove design had the largest failure strain among all designs. To understand more about the mechanism and effect of the mesh design, a finite element analysis (FEA) of the strain concentration around the mesh design was performed and shown in Figure 4d. Other conditions were kept the same while only the mesh shape was changed. When a piece of square mesh was added to the substrate, the

highest strain area shifted to the four corners of the mesh, which left the middle area (where the interconnects are) lower strain at ~0.67. With a shallow cove shape mesh layer added, the strain distributed more around the four end points of the mesh (~0.98) while keeping the center cove area at a lower strain level (~0.52). The deeper cove design concentrated more stress around the end points and lowered the strain (~0.37) at the center area more than the shallow cove design. With this novel cove mesh island multilayer structure, most of the strain generated during stretching would be loaded around the tip area of the mesh, and the interconnects were protected with less strain, which ensured a significantly higher ultimate failure strain of the circuit.

The fabrication process of the interconnects is stated below. The cleaned and dried substrate was placed on the glass slide to ensure flatness. A designed mesh was placed on top of the conductive gold where SMD was going to be mounted. Sliced thin scotch tapes are attached to the side of the mesh to anchor it in place. Silver epoxy was mixed, prepared, and applied to the pre-cut hole on the mesh; electronic components were then aligned and placed on top of the mesh. Then a piece of glass slide is stacked on top with some pre-applied pressure and fixed to the bottom glass slide with scotch tape. The purpose of the top glass slide was to apply constant pressure and force all layers in close contact during the epoxy-heated curing process under 100 °C for 1 hour. After cure, the top glass slide and anchor scotch tape on the mesh were removed. Finally, PDMS was prepared as previously mentioned and spin-coated onto the substrate at 500 RPM for 30 seconds. The PDMS was vacuumed for 10 minutes and cured under 60°C for 1 hour.

4.3: Fatigue Test

The durability of the surface-mounted resistor device was also testified via various strain tests. The device was stretched up to 80 percent strain without noticeable breakage or change in resistance at each strain (Figure 5a). A cyclic test was performed on this device: the device was stretched 30% more than 1000 times (Figure 5b and 5c). The cyclic test demonstrated a stable baseline and consistent waveform. To visualize the durability of the device, a circular LED array (7 LEDs with mesh composite interconnects, Figure 5d) was fabricated and stretched up to 50% strain. Video is recorded with the test simultaneously. The pixel intensity of the LEDs was extracted from each picture taken at each strain percentage and analyzed, which showed no perceptible brightness change (Figure 5e). In summary, the LED and resistor device demonstrated that SMD with the nylon mesh could be a generic way of making wearable devices.

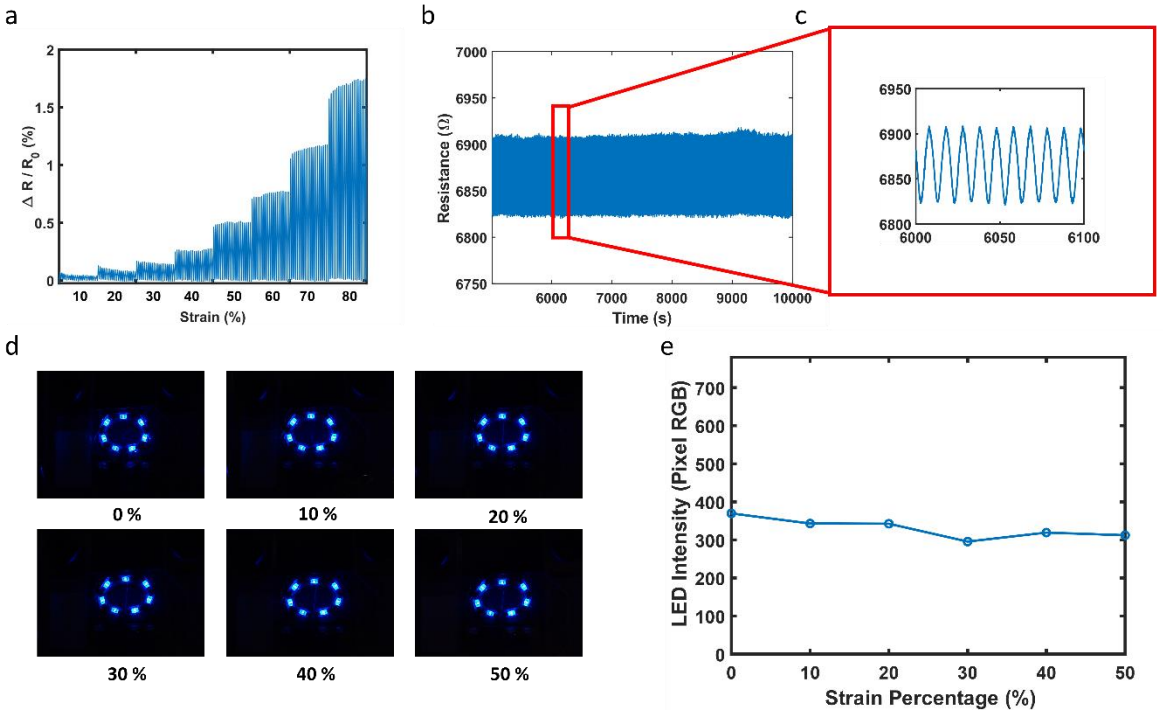

Fig.5(a) Resistance % change at different strain. b) Fatigue test for resistor design. (c) Insert of fatigue test. (d) LED intensity at different strain. (e) Average LED intensity change over different strains.

4.4: Stretchable Circuit Board Applications

Inspired by Chu's previous work[10], a novel fully stretchable wireless respirational sensor is fabricated. From previous work, it was proved that the sensor's strain was dynamically correlated to the respirational pattern. The SCB contains a Bluetooth module and a voltage divider. The entire system was powered by a 3.3 V battery and did not require an external power source. Compared to the resistance of the resistor, the resistance of the Bluetooth module was ~4 MΩ, which was ~100 folds higher. Thus, the relationship among voltage could be described by Ohm's Law as the following equation:

$$V_{sensor} = \frac{V_{total}}{R_{sensor} + R_{fix}} \cdot R_{sensor}$$

where V_{sensor} represented voltage across the sensor, V_{total} represented the voltage across the entire system, R_{sensor} represented the resistance of the

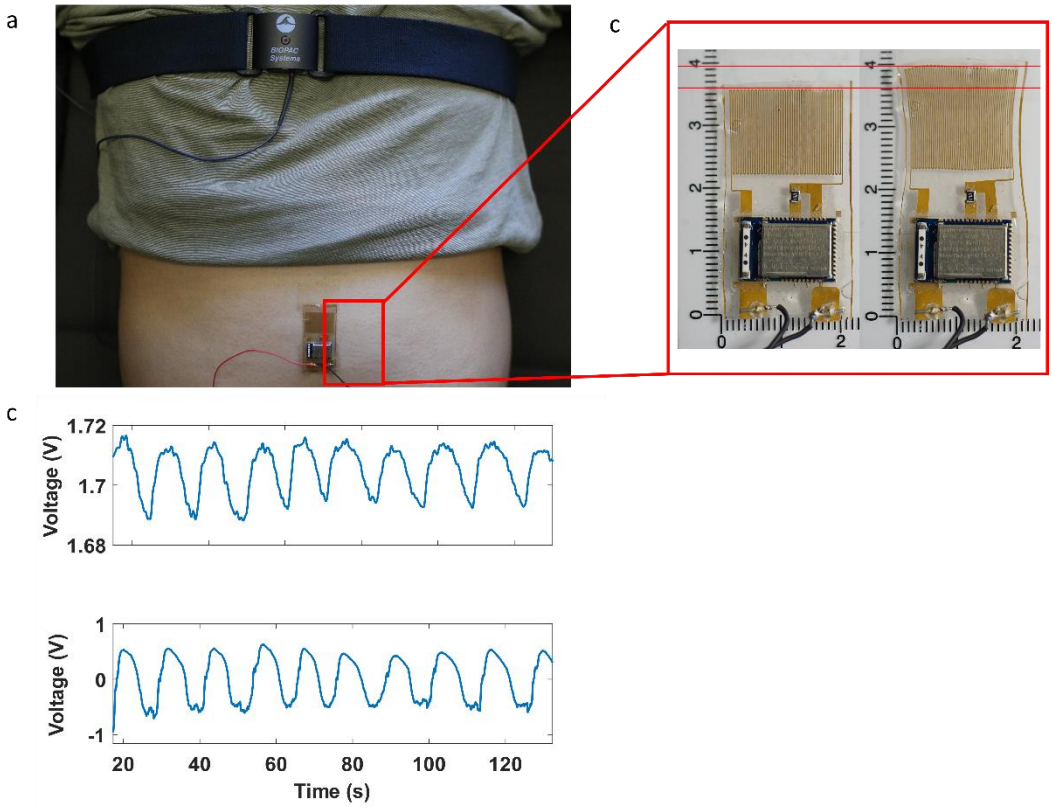

Fig.6(a)Respiration device on the subject (b)Respiration device at different strains when stretched. (c) Comparison of BIOPAC and our respiration device.

fixed resistor. The resistance of the sensor could be calculated as:

$$R_{sensor} = \frac{R_{fix} \cdot V_{sensor}}{V_{total} - V_{sensor}}$$

The Bluetooth module acquired the voltage across the sensor and sent the information to any connected Bluetooth devices. The entire circuit board was attached to the human subject's abdomen via KT tape on its two ends, while the sensor part could be stretched freely along with the movement of the abdomen. As shown in Figure 6b, when the subject inhaled (left picture), due to abdomen expansion, the sensor would be stretched, and resistance would increase; when the subject exhaled (right picture), the sensor would relax back to its original status, and resistance would decrease. To verify whether the sensor was tracking the movement of the abdomen correctly, a time-synchronized video was recorded along with the sensor signal recording simultaneously. The video was analyzed by tracking the pixel movement of the abdomen frame by frame. The plot in Figure 6c showed a good correlation between the abdomen movement and the sensor voltage change.

A fully stretchable two-lead ECG circuit board was designed and tested as the next application. First, a differential amplifier increased the impedance of two signal inputs from the subject and amplified the difference between the two inputs. Then the amplified differential signal was passed through an active band pass filter with a passing frequency between 0.05 Hz and 32.88 Hz. The differential amplifier had a gain of 24.4, and the bandpass filter had a gain of 22. Theoretically, the entire system could amplify the input signal difference with a gain of 537. The simulated signal amplification was indicated in Figure 7c. One of the inputs was grounded, and another one was a sinusoid signal (red line) with 2 mV peak-to-peak amplitude and 10 Hz frequency. The system produced the expected output voltage (blue line) of 1.07 V peak to peak, closely matching the theoretical values. Although it was not expected to stretch the ECG board during normal usage, the stretching of the circuit to different strains (up to 50%) shows negligible effect on the output signal quality. Eventually, the

circuit board was placed on a human subject with three dry electrodes connected (two for signal input and one for ground) and powered by one 3.3 V and one 1.5 V coin battery. In order to verify the accuracy of the Bluetooth module, the output signal was captured by a wired DAQ board and Bluetooth module simultaneously. From Figure 7d, it could be observed that the Bluetooth module was tracking approximately the same result as the wired board, and the QRS complex and T wave were clearly shown in the ECG diagram. As mentioned before, although the overall impedance of the gold wires was higher than other conductive wires[28,76,77], it did not have a noticeable effect on the applications as long as the components' impedances were high enough.

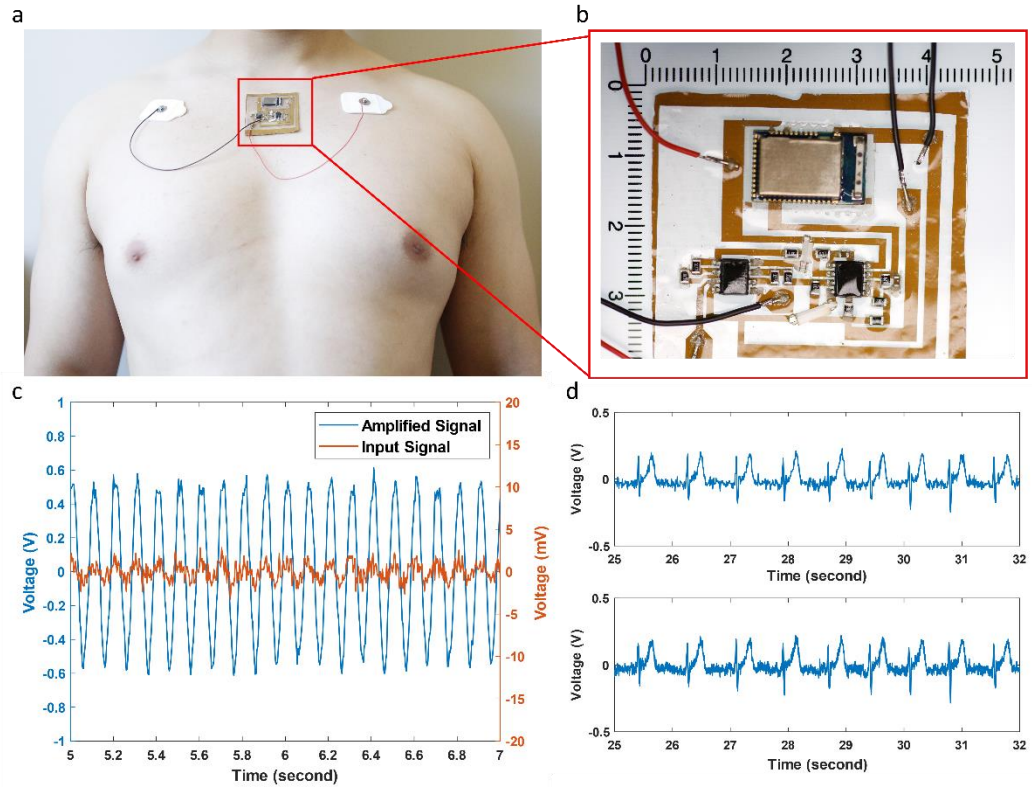

Fig.7(a)EKG device on the subject (b)EKG device at close look. (c) Comparison between input signal and amplified output signals. (d) Human EKG signal acquired by wired device and wireless unit.

4.5: Conclusion

In this work, a novel fabrication method to rapidly and consistently produce SCBs was introduced. Utilizing the commercialized pre-sputtered gold polystyrene sheet saved the sputtering time in the previous fabrication procedure and minimalized batch-to-batch differences. After transferring to a stretchable PDMS substate, the gold could be laser ablated, and the circuit design could be quickly fabricated. The resulting wrinkled gold conductive could tolerate high strain without noticeable resistance change when stretched. Commercialized silver epoxy, along with specially designed nylon mesh, was directly applied to the gold-component interface to create robust and conductive interconnects that ensured a high failure strain of up to 137%. The cyclic stability of the design was up to at least 1000 cycles. The combination of techniques allowed quick and reproducible conversion from traditional PCBs to SCBs.

Although currently, the mesh and SMDs were mounted by hand in the current prototype, they could be modified and adapted to the current PCB fabrication process. The conductive epoxy could be pre-dispensed onto the designed locations, and the pre-cut mesh could be aligned and adhered to the bottom of SMDs. Afterward, the mechanical arm would pick up the SMD with the mesh and locate it in place. After all, components were in place, the entire board would be heat cured, and the encapsulation could be done afterward.

There were several limitations to the current design. The first issue was that the resolution of the circuit design was limited by the laser cutter precision (~100 μm). However, this limitation could be improved if a more advanced and precise laser cutter was used. The second problem was the relatively high resistance of the wrinkled gold film. The resistance of the conductive wire was relatively high compared to other publications. However, the LEDs, respirational device, and ECG board applications still demonstrated reliable performance and negligible change in signals at different strains.

Overall, this novel fabrication method suggests that it may open new avenues for developing stretchable circuit boards by simplifying board fabrication and toughing interconnects.

Chapter 5: Sleep Data Analysis and Machine Learning

The ultimate goal of my work is to integrate sensors and acquisition devices with machine learning for continuous monitoring. In the previous chapters, I demonstrated that it is feasible to fabricate stretchable sensors with an integrated wireless acquisition device. In this chapter, to demonstrate the ability of machine learning for home monitoring, I analyze sleep data from a sleep clinic. I demonstrate how a machine learning model can be used to process the data faster and more accurately. I examine 5 different time series signals: photoplethysmography (PPG) channel, respiration flow rate channel, two respiration effort channels, and R-R interval channel calculated from ECG channel from sleep patients. The result turns out that the combination of PPG signals and respiration effort channels produces the best model among all the different combinations.

5.1: Introduction and Motivation

Sleep is a fundamental aspect of human physiology that is essential for overall health and well-being[78]. During sleep, the brain and body undergo a complex series of processes that are critical for physical and cognitive restoration[79]. Sleep is composed of different stages, each of which is characterized by distinct patterns of brain activity and physiological changes[80]. These stages are generally classified into non-rapid eye movement (NREM) and rapid eye movement (REM) sleep[81] . NREM sleep is further divided into three stages based on the presence of specific brain wave patterns[82], while REM sleep is characterized by rapid eye movements, vivid dreaming, and physiological changes such as increased heart rate and breathing[83].

The different sleep stages play important roles in various aspects of human physiology, including memory consolidation[84], hormone regulation[85], and immune function[86]. Additionally, specific sleep activities such as obstructive sleep apnea[87], sleepwalking[88], and REM sleep behavior disorder (RBD)[89] can provide insights into underlying neurological conditions.

The gold standard for detecting sleep stages is polysomnography (PSG), which involves recording various physiological parameters during sleep, including electroencephalogram (EEG), electromyogram (EMG), and electrooculogram (EOG). The EEG records brain activity, while the EMG records muscle tone, and the EOG records eye movement. These parameters are analyzed by a trained sleep technologist or computer algorithm to determine the different stages of sleep.

Deep learning has become a powerful tool in recent years, and there are many researchers utilizing different types of neural networks to classify sleep stages[90–93]. The researchers that show very accuracy are using PSG signals, including EEG, which is only available in the sleep lab. However, in recent years, various wearable devices, such as wrist-worn actigraphy monitors and headbands, have been developed to detect sleep stages in a non-invasive manner. These devices use various sensors, such as

accelerometers and PPG, to track movement and heart rate, respectively. While these devices are not as accurate as PSG, they provide a convenient and cost-effective means of tracking sleep stages over time. Researchers utilize PPG signals to make predictions on sleep stages and show relatively high accuracies. In order to further improve the accuracy, most of them develop more advanced models.

Besides the PPG signal, respiration is also closely related to the sleep stage and has a significant impact on each other. Sleep is an essential physiological process that is critical for maintaining overall health and well-being, while respiration refers to the process of breathing that supplies the body with oxygen and removes carbon dioxide. During sleep, the respiratory system undergoes changes that are closely linked to the various stages of sleep. The complex interplay between respiration and sleep has been the subject of extensive research, and a better understanding of this relationship is essential for the diagnosis and treatment of various sleep disorders.

During sleep, the respiratory system undergoes significant changes that are closely linked to the various stages of sleep[94]. During non-REM sleep, respiration becomes more regular and efficient, while during REM sleep, it becomes more irregular and prone to interruptions. This is due to changes in the activity of respiratory muscles and the level of carbon dioxide in the body, which are regulated by the central nervous system. These changes in respiration during sleep are critical for maintaining normal oxygen and carbon dioxide levels in the body.

In addition, the relationship between respiration and sleep is particularly relevant in the context of sleep disorders such as obstructive sleep apnea (OSA). OSA is a common disorder characterized by repeated episodes of partial or complete obstruction of the upper airway during sleep, leading to disrupted respiration and frequent arousals from sleep. The frequency and severity of apnea events in OSA are strongly linked to the sleep stage, with the majority of events occurring during REM sleep[95]. This highlights the importance of understanding the relationship between respiration and sleep stages in the

diagnosis and treatment of OSA.

In this study, I am demonstrating a different way to improve sleep stage prediction with signals collected by wearable devices. Instead of a PPG signal, there are other channels, such as respiration flow and respiration effort sensors, for in-home sleep studies. The study illustrates that with additional respiration channels, the model achieves better overall performance.

5.2: Data Set Description

The dataset used in this study consisted of deidentified polysomnography (PSG) recordings from the UCI Sleep Center. The files were deidentified and exported into European Data Format (EDF), preserving only the primary diagnosis of the record. All clinical studies were conducted in the UCI Sleep center according to the American Academy of Sleep Medicine (AASM) practice parameters for in-lab sleep studies using a Natus SleepWorks PSG ® acquisition system.

Sleep staging was performed by one of two registered polysomnography technologists who participated in interscorer variability quality assurance as required by AASM. All studies were overread by one Board certified Sleep Physician (RNK). Scoring was done according to the AASM scoring manual (ref).

The dataset included 123 PSGs. 33 had OSA (+ about 20 from Vena files). The remainder (20+20+ a few from Vena files) had other sleep disorders

5.3: Method

5.3.1: EEG arousal data set preparation:

The flow for data pre-processing is illustrated in figure 8. The data is first Z-score normalized to achieve a mean of 0 and standard deviation of 1, then it is downsampled to 64 Hz. The data is segmented into 30 seconds duration according to EEG arousal event labels. Finally, different channels are concatenated to create input data.

123 subjects' data is used to predict the existence of EEG arousal events. The existence of arousal events is manually scanned and determined based on EEG channels by trained technicians. In this study, five channels are used to determine the sleep stages, including a photoplethysmogram (PPG) signal from a finger pulse oximeter, respiration flow rate, respiration effort sensor on the chest, respiration effort sensor on the abdomen, and RRI calculated from ECG channel. Each data point contains 5 channels of 30 seconds of information, and all channels are down-sampled from 512 Hz to 64 Hz to increase calculation efficiency. The length of each channel in each data point is 1921. The start point of each event data point is 15 seconds before the arousal event label time; the end point is 15 seconds after the arousal event label time. The baseline is defined as any random 30 seconds periods

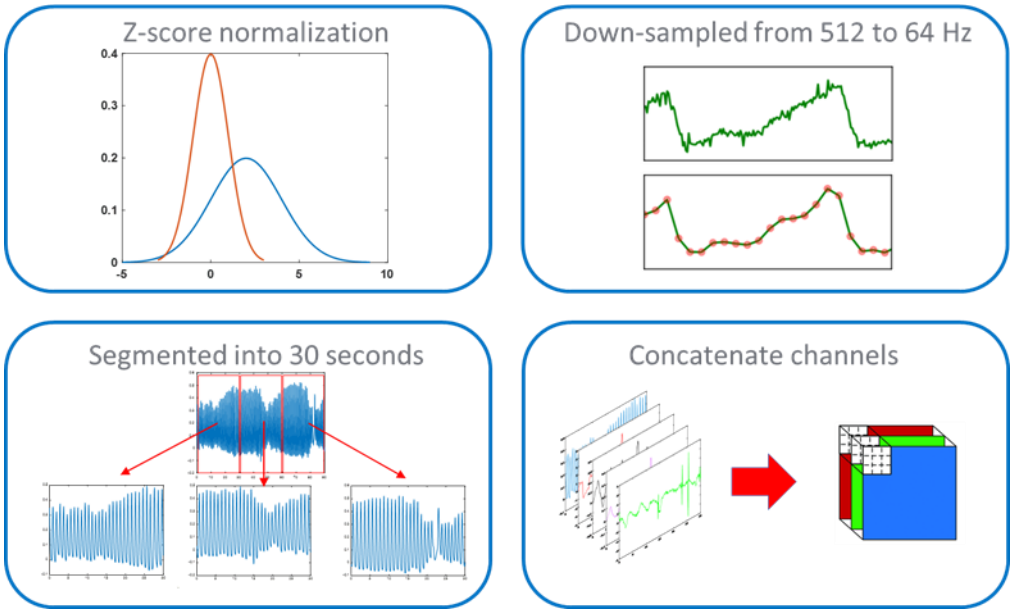

Fig.8 Four major steps to pre-process the data: Z-score normalization, down-sample to 64 Hz, segment into 30 seconds, concatenate different channels

that have no arousal events and no motion artifacts. The entire data preparation is performed in MatLab R2022b.

RR interval is calculated from the ECG channel by referring to Geng et al. and Wei et al. [96,97]. Briefly, 5 minute ECG signal prior to the 30 seconds sleep stage is selected. If there is discontinuity or artifacts, this 5-minute segment is abandoned. All R peaks within the 5 minutes are extracted, and RR intervals are calculated except the last R peak. The equation is shown below:

$$RRI_i = R_{i+1} - R_i$$

Because the RRI is not continuous or equally distanced, a spline interpolation is applied to the signal to create an equally-spaced input signal. Because the RRI is different among different patients, Z-score normalization is performed for each 5-minute section. The RRI signal has the same length as other channels.

In order to train the model to pay more attention to the shape and relative shape change of the signal instead of the absolute value of each channel, Z-score normalization is performed on all data points. For example, every data point is subtracted by the mean value of the channel for the entire recording duration and then divided by its standard deviation of the channel for the entire recording duration. After the normalization, every channel has a mean of zero and a standard deviation of 1, although, within each segment, this may not be the case. After normalization, every data point has a dimension of 5 x 1921 (channel x timestep). Data is examined to remove potential motion artifacts. A peak detection method is used. Within the 30 seconds period, if there are less than 20 peaks or more than 60 peaks exist in the PPG signal (less than 40 or more than 120 heartbeats per minute during sleep are highly uncommon), this entire data point is excluded from the experiment. No further data pre-processing is performed besides normalization and the number of peaks threshold cutoff.

The complete data set contains 22772 data points with 11210 (49.23%) events and 11562 (50.77%) baselines. The data set is split into 80% (18217) training set, and 20% (4555) test set randomly.

5.3.2: Sleep stage data set preparation:

The flow for data processing is similar to EEG arousal event detection. The data is first Z-score normalized to achieve a mean of 0 and standard deviation of 1, then it is downsampled to 64 Hz. The data is segmented into 30 seconds duration according to sleep stage labels provided by sleep technicians. Finally, different channels are concatenated to create input data.

123 subjects' data are used in the sleep stage prediction. Each subject's sleep stage is manually labeled every 30 seconds based on EEG and EMG channels by trained technicians. In this study, five channels are used to determine the sleep stages, including a photoplethysmogram (PPG) signal from a finger pulse oximeter, respiration flow rate, respiration effort sensor on the chest, respiration effort sensor on the abdomen, and RRI calculated from ECG channel. The entire data preparation is performed in MatLab R2022b. Each data point contains 5 channels of 30 seconds of information, and all channels are down-sampled from 512 Hz to 64 Hz to increase calculation efficiency. The length of each channel in each data point is 1921.

In order to train the model to pay more attention to the shape and relative shape change of the signal instead of the absolute value of each channel, every 30 seconds segment is normalized to itself. For example, every data point is subtracted by its mean value within 30 seconds and then divided by its standard deviation within 30 seconds. After the normalization, every channel has a mean of zero and a standard deviation of 1. After normalization, every data point has a dimension of 5 x 1921 (channel x timestep). Data is examined to remove potential motion artifacts. A peak detection method is used. Within the 30 seconds period, if there are less than 20 peaks or more than 60 peaks exist in the PPG signal (less than 40 or more than 120 heartbeats per minute during sleep are highly uncommon), this entire data point is excluded from the experiment. No further data pre-processing is performed besides normalization and the number of peaks threshold cutoff.

The complete data set contains 99981 data points. In these 99981 data points, 24.54% (24541) are wake stage, 5.80% (5798) are N1 stage, 40.02% (40017) are N2 stage, 15.70% (15770) are N3 stage, 13.86% (13855) are REM stage. The data set is split into 80% (80010) training set, and 20% (19971) test set randomly.

5.3.3: Neural network architecture and training process

Inspired by Korkalainen et al. [90], we implement a convolutional neural network (CNN) connected with a bidirectional long short-term memory network (BiLSTM) to classify the sleep stages. The structure is presented in figure 9. CNN is used to learn useful information from the shape, such as the relative

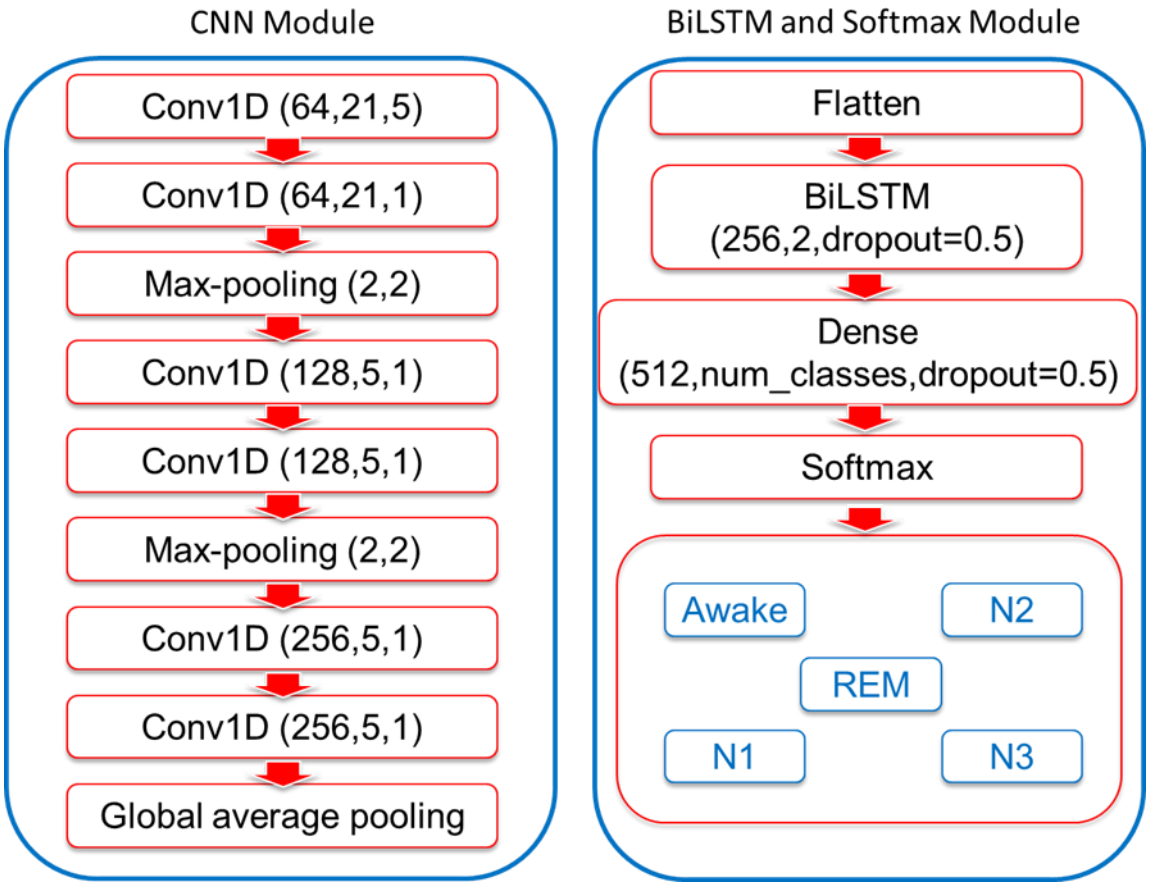

Fig.9 Architecture of the neural network. It contains one CNN module and one BiLSTM module.

height of each peak, the slope of the peak, or whether the peak is flatter or sharper. BiLSTM is used to learn temporal information within the 30 seconds window, such as the time lag between the first and second peaks. There are 3 independent classification systems, 3 stages (wake, Non-REM, REM), 4 stages

(wake, N1+N2, N3, REM), and 5 stages (wake, N1, N2, N3, REM) systems. Furthermore, we modify the input channels to be different combinations of the original input to test which input combination produces the best result. The different combinations are shown in figure 10. In total, we test 8 different signal combinations and compare the results among them. The model architecture is the same for

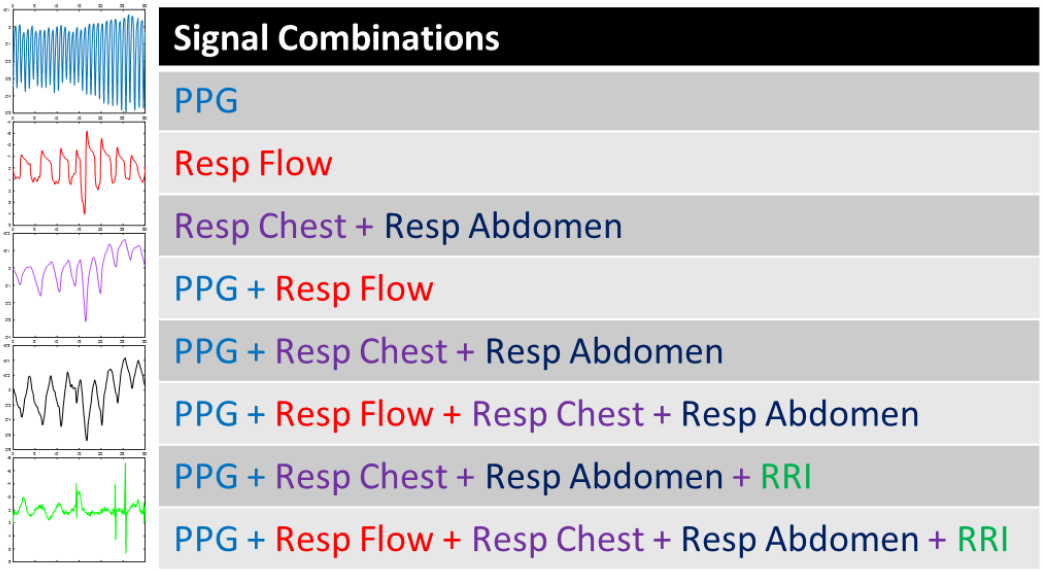

Fig.10 Different signal combinations that used in the model

different models except for input dimensions and output dimensions. The network is implemented in Python 3.7

with PyTorch 1.13.1.

In the CNN section, there are six 1-D convolutional layers, two max-pooling, and one global average pooling. Each 1-D convolutional layer is followed by a 1-D batch normalization and a rectifier linear unit (ReLU) for activation. There is a max-pooling layer after the second and the fourth convolutional layer. A global average pooling is connected at the end of CNN. After the global average pooling, the output is fed into BiLSTM. The BiLSTM contains 2 layers of 256 units with a dropout rate of 0.5 to reduce overfitting. The output from the last layer at the last timestep is fed into a fully connected layer to make a final decision with the dimensions equal to the number of predicted classes. The fully connected layer has a dropout rate of 0.5.

The data is randomly divided into mini-batches with a batch size of 32 during training. Each batch is fed into the network in sequence. The original input dimension is 32 samples x # of channels x 1921 timestep, while the output dimension is 32 samples x # of categories. The category that has the highest probability will be the final categorical prediction. During training, categorical cross-entropy loss and Adam optimizer are used. An L2 regularization term is also added to the optimizer to reduce potential overfitting. The initial warm-up learning rate is 0.001 to avoid potential local minimum, and after 15 training epochs, the learning rate is decreased to 0.0001 for further fine training. After each epoch is trained, the model is evaluated on the test set and training set. The training is done after 50 epochs. The model that has the highest test accuracy among 50 epochs will be saved.

5.3.4: Statistical terms

In this study, 5 scores are used to describe the performance of the model. The first score is accuracy, which is:

$$accuracy = \frac{total\ number\ of\ correct\ prediction}{total\ number\ of\ prediction}$$

The second score is precision, which is:

$$precision = \frac{number\ of\ true\ positive}{number\ of\ true\ positive + number\ of\ false\ positive}$$

The third score is recall, which is:

$$recall = \frac{number\ of\ true\ positive}{number\ of\ true\ positive + number\ of\ false\ negative}$$

The fourth score is F1 score, which is:

$$F1 = \frac{2 \times precision\ \times recall}{precision + recall}$$

The fifth score is cohen's kappa score, which is:

$$\kappa = \frac{p_0 - p_e}{1 - p_e}$$

Moreover, because the precision, recall, and F1 score are class dependent, there are weighted-precision, weighted-recall, and weighted-F1 scores calculated to provide a better model overall score.

5.4: Results

For the EEG arousal event detection and sleep stage classification, I alternate the combination of input channels and compare the performances of different combinations. These combinations include PPG alone, respiration flow alone, respiration effort alone, PPG + respiration flow, PPG + respiration effort sensor, PPG + respiration flow + respiration effort sensor, PPG + respiration effort sensor + RRI, and PPG + respiration effort sensor + respiration flow + RRI.

I perform four different classification tasks for sleep stage detection. The first one is wake and sleep classification; the second one is wake, non-REM, and REM sleep; the third one is wake, N1 + N2, N3, REM sleep; the fourth one is wake, N1, N2, N3, REM sleep. Within each classification task, the combinations of input channels are the same as the EEG arousal event.

5.4.1: EEG arousal event detection

The summary of the EEG arousal event is shown in the table below. The best model is marked in red color. The confusion matrix of the best model is shown in figure 11. The best model is the one using

Precision Recall F1 (Kappa)	PPG Alone (reference)	PPG	Resp Flow	Resp Chest Resp Abd	PPG Resp Flow	PPG Resp Chest Resp Abd	PPG Resp Flow Resp Chest Rest Abd	PPG Resp Chest Rest Abd RRI	PPG Resp Flow Resp Chest Rest Abd RRI
EEG arousal	N/A	72.72 72.06 71.84 (0.44)	62.93 62.88 62.84 (0.26)	62.46 62.19 61.96 (0.24)	73.12 73.12 73.11 (0.46)	74.89 74.41 74.29 (0.49)	72.96 72.04 71.74 (0.44)	74.26 71.48 73.50 (0.47)	73.61 73.48 73.45 (0.47)

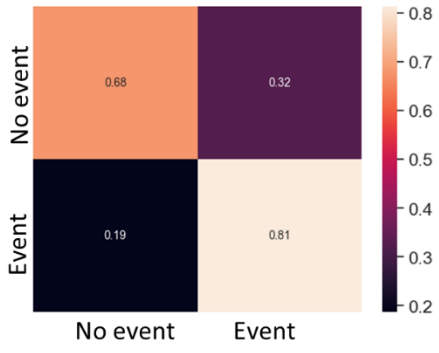

Fig.11 Confusion matrix for EEG arousal event classification

PPG and two respiration effort sensors. By comparing the performance between PPG and PPG + effort sensors, we can observe most of the prediction power comes from the PPG channel, but by adding the effort sensor's channel, the performance is still increased. The confusion matrix tells that the model is able to retrieve 81% of events correctly but only 68% of the baseline events. This indicates the model needs improvement on baseline (no events).

5.4.2: Wake and sleep classification

This model is a 2 stages classifier (wake, sleep). The best model uses PPG, flow, and 2 effort sensors. The input dimension is 32 x 4 x 1921 (batch size x # of channels x timestep). The output's dimension is 32 x 2 (batch size x # of classes). This model has a test accuracy of 94.89%. The precision, recall, and F1 score for each class are shown below: for wake, 90.31%, 82.96%, and 86.48%; for sleep, 95.71%, 97.72%, and 96.70%. The weighted precision, weighted recall, and weighted F1 score are

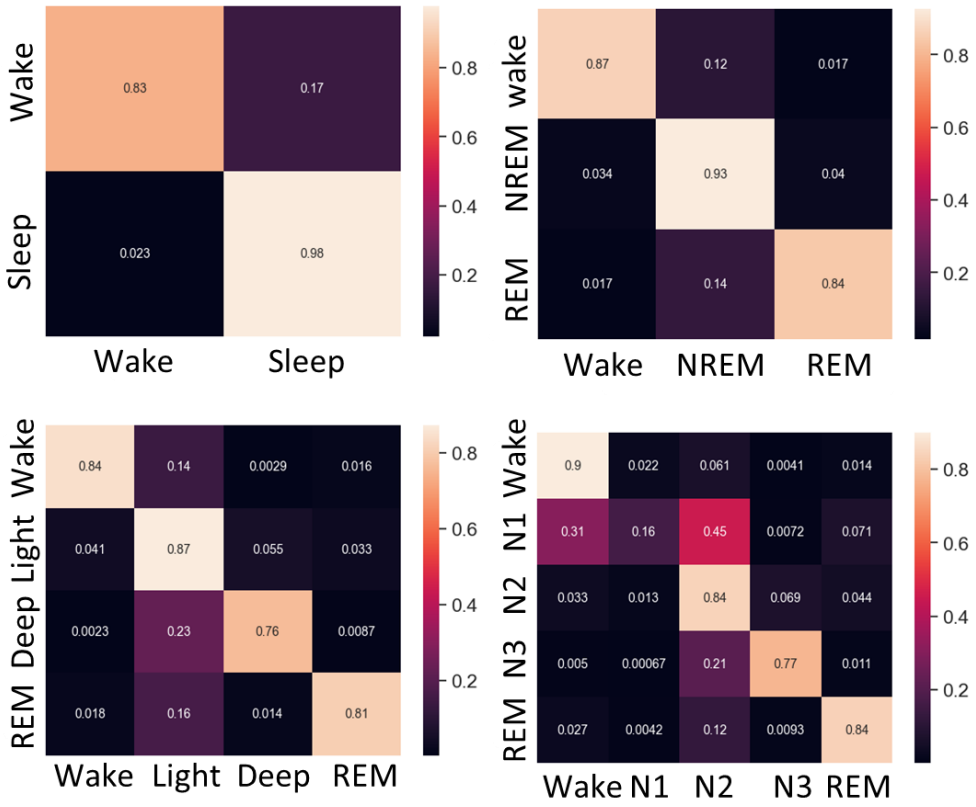

Fig.12 Confusion matrix for 2 stages, 3 stages, 4 stages, and 5 stages classification

94.61%, 94.70%, and 94.62%. The kappa value is 0.83. The normalized confusion matrix is shown in figure 12a. From the confusion matrix, we can see that the model is able to predict 98% of the sleep correctly but only 83% of wake correctly. One potential reason is the data screw. In the entire data set, only 24.54% are wake stage. Because the model is trained on much fewer wake data, it will have worse performance on the wake stage.

5.4.3: Wake, non-REM, and REM classification

This model is a 3 stages classifier (wake, Non-REM, REM). The best model uses PPG, flow, and 2 effort sensors. The input dimension is 32 x 4 x 1921 (batch size x # of channels x timestep). The output's dimension is 32 x 3 (batch size x # of classes). This model has a test accuracy of 90.59%. The precision, recall, and F1 score for each class are shown below: for wake, 88.63%, 87.45%, and 88.04%; for Non-REM, 91.67%, 94.84%, and 93.23%; for REM, 88.13%, 76.99%, and 82.18%. The weighted precision, weighted recall, and weighted F1 score are 90.51%, 90.59%, and 90.47%. The kappa value is 0.82. The normalized confusion matrix is shown in figure 12b. We can see REM and Wake's stages are predicted with less performance. In the dataset, 24.54% are wake stage, and 13.86% are REM stage, so the worse performance is reasonable.

5.4.4: Wake, light sleep, deep sleep, and REM classification

This model is a 4 stages classifier (wake, light sleep (N1 + N2), deep sleep (N3), REM). The best model uses PPG and 2 effort sensors. The input dimension is 32 x 3 x 1921 (batch size x # of channels x timestep). The output's dimension is 32 x 4 (batch size x # of classes). This model has a test accuracy of 83.69%. The precision, recall, and F1 score for each class are shown below: for wake, 88.70%, 84.43%, and 86.52%; for light sleep, 81.31%, 87.21%, and 84.16%; for deep sleep, 82.80%, 76.35%, and 79.45%; for REM 86.19%, 80.57%, and 83.28%. The weighted precision, weighted recall, and weighted F1 score are 83.84%, 83.69%, and 83.67%. The kappa value is 0.76. The normalized confusion matrix is shown in

figure 12c. 24.54% are wake stage, 45.82% are light sleep stage, 15.70% are deep sleep stage, and 13.86% are REM stage.

5.4.5: Wake, N1, N2, N3, and REM classification

This model is a 5 stages classifier (wake, N1, N2, N3, REM). The best model uses PPG and 2 effort sensors. The input dimension is 32 x 3 x 1921 (batch size x # of channels x timestep). The output's dimension is 32 x 5 (batch size x # of classes). This model has a test accuracy of 80.69%. The precision, recall, and F1 score for each class are shown below: for wake, 84.41%, 89.94%, and 87.09%; for N1, 42.99%, 16.15%, and 23.48; for N2, 79.34%, 84.13%, and 81.67%; for N3 81.55%, 77.31%, and 79.38%; for REM 82.88%, 83.81%, and 83.34%. The weighted precision, weighted recall, and weighted F1 score are 79.51%, 80.69%, and 79.74%. The kappa value is 0.73. The normalized confusion matrix is shown in figure 12d.

In the data set, 24.54% (24541) are wake stage, 5.80% (5798) are N1 stage, 40.02% (40017) are N2 stage, 15.70% (15770) are N3 stage, 13.86% (13855) are REM stage. The small percentage of N1 results in low performance in the N1 stage. Another finding is the model classifies 31% of N1 as wake, while 45% of N1 as N2. This potentially indicates it might be true that N1 is the stage when the person starts to fall asleep, and it is a stage between wake and N2. This transition stage may be very similar to wake and N2 as well, and this might be another reason for bad N1 performance. For N3 stages, 21% are classified as N2, and 7% of N2 are classified as N3. A good way to improve the model is trying to look into those incorrect predictions and examine them manually. Overall, the confusion matrix gives a good understanding of how we can improve the model in the future.

5.4.6: Precision, recall and F1 score summarization table for sleep stages

The averaged precision, recall, F1, and Cohen's Kappa are shown in the table below. In the table, each row represents a different classification task, and each column represents a different input signal

combination. The best-performing model is marked in red. The models that contain RRI information are in blue.

Precision Recall F1 (Kappa)	PPG	Resp Flow	Resp Chest Resp Abd	PPG Resp Flow	PPG Resp Chest Resp Abd	PPG Resp Flow Resp Chest Rest Abd	PPG Resp Chest Rest Abd RRI	PPG Resp Flow Resp Chest Rest Abd RRI
Wake, Sleep, 2 stages	91.03 91.24 90.77 (0.70)	85.40 86.01 85.61 (0.55)	91.68 91.92 91.66 (0.74)	91.84 91.36 91.53 (0.75)	93.73 93.86 93.74 (0.80)	94.61 94.70 94.62 (0.83)	91.74 91.76 91.75 (0.75)	92.96 92.66 92.77 (0.78)
Wake, Non-REM, REM, 3 stages	86.35 86.43 86.39 (0.74)	74.90 75.37 74.64 (0.50)	87.63 86.99 87.18 (0.76)	85.20 84.41 84.67 (0.71)	89.34 89.42 89.28 (0.79)	89.41 89.51 89.35 (0.79)	87.57 87.54 87.56 (0.76)	86.13 85.56 85.73 (0.73)
Wake, N1+N2, N3, REM, 4 stages	78.82 78.16 78.14 (0.69)	64.01 59.36 60.02 (0.44)	81.87 81.85 81.82 (0.73)	76.54 75.13 75.43 (0.64)	83.44 83.39 83.37 (0.76)	82.71 82.61 82.62 (0.75)	79.30 79.28 79.23 (0.70)	79.59 79.04 78.84 (0.69)
Wake, N1, N2, N3, REM, 5 stages	74.53 74.40 73.75 (0.66)	61.33 62.18 60.83 (0.46)	78.23 79.43 78.42 (0.72)	74.44 74.97 74.00 (0.64)	78.96 79.99 79.23 (0.72)	79.36 79.51 79.23 (0.71)	78.31 79.88 78.48 (0.71)	74.23 73.69 73.74 (0.64)

5.5: Discussion

Although there is an intrinsic relationship between sleep stages and respiration, nobody analyzes this relationship. Traditionally, the PPG signal is a popular alternative that many researchers use to predict sleep stages besides EEG signals. The data presented in the previous section demonstrate that instead of the PPG signal, respiration signals and sleep stages also have a correlation and lead to higher model performance. For all 4 different classification tasks, the precision, recall, and F1 scores of respiration effort-only models are higher than PPG-only models (the third column and the first column). Moreover, when combining PPG and effort sensors, the model performs better than any of the signals alone.

From the summarization table, one trend is obvious. Looking at each column, all the performance numbers decrease when the model tries to predict more stages. This intuitively makes sense because more categories will increase the classification difficulty.

Another finding is the best models are either PPG + respiration effort sensors or PPG + respiration effort sensors + flow sensors. The performance of these two combinations is higher than any other signals alone or other combinations. The respiration flow channel does not add too much value to the model. Thus, for the sake of fewer inputs, the respiration flow channel is not necessary for this study. But it might still be useful for other tasks.

Another finding is that more input channels do not always provide better results. From the results, it can be observed that the models containing RRI channel perform worse than the model without RRI channels. Adding the RRI channel to the model will decrease the model's performance. One possible reason for this is due to the mechanism of CNN. At each CNN layer, there are multiple kernels with different parameters. However, all the kernels are shared among all input channels. That is saying, for each kernel, the results are the summation of all channels, and each channel has the same weight percentage. In this case, if one input channel contains more noise, the addition of this channel will add

more noise to the final results. The RRI channel is the one that contains noise and worsens the overall performance.

5.6: Conclusion

5.6.1: Summary

I demonstrate that EEG arousal events can be detected with PPG and respiration channels accurately. Different sleep stages can also be classified accurately. It is not necessary to perform feature extraction from the raw signal because any feature extraction may cause the loss of information. Only Z-score normalization is necessary for data pre-processing. There is still improving the potential for the models, especially for multi-stages. Data screw is a common problem for all sleep stages data sets. In this study, 24.54% (24541) are wake stage, 5.80% (5798) are N1 stage, 40.02% (40017) are N2 stage, 15.70% (15770) are N3 stage, 13.86% (13855) are REM stage. It can be observed that F1 scores from low to high are N1, N3, and REM. All models perform worst on N1 stage prediction due to a lack of N1 data. The performance on the REM stage is also lower than in other stages.

This study still makes it possible to monitor the sleep status of patients at home without other PSG channels. With PPG and respiration effort sensors, the model is able to differentiate whether the patient is awake or asleep with good accuracy. It can also predict if the patient has an EEG arousal event or not.

5.6.2: Future works

The study shown in this chapter demonstrates that with the deep learning model, detection of EEG arousal events and sleep stages is possible for at-home study. More patients can potentially benefit from this study. They do not need to go to the sleep lab, and less equipment is needed to collect the sleep data. One challenge is the model's accuracy, especially for fine stages differentiation such as N1 and REM. This could be improved by collecting more data for model training. A better model will also help. Currently, many researchers have already demonstrated that a transformer-based natural language model could be applied to time series prediction[98–101]. The transformer-based model tends to work better than CNN + BiLSTM-based model for time series prediction.

Chapter 6: Discussion and future prospect

6.1: Summary

The utilization of wearable sensors for tracking human vital signs necessitates consideration of patient and hardware factors, which give rise to distinct requirements. With regard to the sensors themselves, it is crucial that the entire system is soft and flexible enough to mold to the skin. This is crucial not only for ensuring patient comfort but also for obtaining accurate signals. On the other hand, patients must have a solid grasp of human anatomy in order to determine the type and quality of signals that can be obtained from the body. Our aim in this study was to provide initial findings in both of these domains, with the expectation that they will ultimately lead to the development of comprehensive human vital signs monitoring system.

In chapter 2, I discuss a novel method to fabricate a stretchable conductive substrate. It is a method that is improved from Khine lab's previous wrinkle surface fabrication process. More specifically, we outsource the sputtering process and get rid of the shadow mask method. Laser ablation is used to create patterns on the substrate. This process saves a lot of time and increases production efficiency by fabricating in parallel.

In chapter 3, a process of fabricating super-sensitive strain sensors is explored. We tune the sensor's sensitivity by modifying the metal layer's thickness and composition substrate layer's stiffness. With the improved sensitivity up to 5 um, the sensor is able to track micro-movements. Additionally, the sensor is able to detect the opening and closing of valves.

In chapter 4, I introduce a new approach to creating stretchable circuit boards (SCBs) that is both rapid and consistent. The method involves using a pre-sputtered gold polystyrene sheet, which eliminates the need for sputtering time and minimizes differences between batches. The gold layer can then be laser ablated and transferred onto a stretchable PDMS substrate to quickly create the circuit

design. The resulting wrinkled gold conductive layer can withstand high levels of strain without experiencing any noticeable change in resistance when stretched. To create durable and conductive interconnects that can withstand strains up to 137%, a commercialized silver epoxy and specially designed nylon mesh were directly applied to the interface between the gold component and the stretchable substrate. Additionally, the cyclic stability of the design was tested and shown to last for at least 1000 cycles. By combining these techniques, this method enables a rapid and reproducible transition from traditional PCBs to SCBs. Different SCBs that can measure human EKG and respiration rate are fabricated to demonstrate the functionality of the SCBs.

In chapter 5, to demonstrate the power of adding machine learning to our sensors, I develop a method using deep learning to classify sleep stages and detect arousal events. Without using traditional EEG signals that can be collected only in a sleep lab, using PPG and respiration channels that are accessible at home can produce reliable and accurate predictions. When combining PPG and the respiration channel, the performance of the model will get further boosted compared to any single input channel alone. This model only needs to perform Z-score normalization on the input data and cut into 30 seconds duration. No complicated feature extractions are needed for this model. This easy approach allows patients to be monitored at home yet still allows automated prediction of their sleep stage and arousal event accurately.

6.2: Future works

The work done in this dissertation includes different directions of wearable devices. There are potential works in several different directions that can be continued in the future.

The first direction is the hardware part of wearable devices. Even though I have demonstrated the robustness and functionality with multiple applications, there are still large many that can be improved and built upon. One important potential work is to implement the multi-layer structure.

Currently, all devices are single-layer structures, which makes it hard to extend the functionality. More functionalities mean more components, which need more space. With the current structure, the only way is to increase the surface area and mount more components. However, if the device can be made with multiple layers, the surface area will remain the same, but the number of components will increase.

The second direction is the method to process the signal collected from the patient. I already demonstrated with home-accessible signals, the model is able to differentiate different sleep stages with high accuracy. The model is also able to detect EEG arousal events. However, I do not investigate other events, such as apnea and hypopnea. Moreover, these events can be further divided into finer classes, such as central apnea and obstructive apnea. More detailed data is needed to study these events. As mentioned in the previous chapter, a transformer-based NLP model could be used to increase model performance as well.

6.3: Future prospects

In order for wearable technology to become ubiquitous in the future, there are numerous obstacles that must be overcome. Currently, very few soft electronic systems can operate without being integrated with a traditional PCB in order to connect to existing wireless infrastructure. Furthermore, soft electronic systems that have managed to be successfully integrated often require a complex fabrication process, which makes scaling up production difficult. To make soft wearable sensors more widespread, a method must first be developed that can integrate all the necessary components of a circuit, especially existing SMDs, while also being scalable. The fabrication method used in this dissertation has the potential to be scalable through a roll-to-roll process. Without a good manufacturing plan, soft wearable devices will likely remain restricted to the academic realm. Additionally, the data acquired must be of high quality and actionable, meaning that methods for

eliminating motion artifacts or identifying poor-quality data must be developed. High-quality data can then be processed by machine learning algorithms to identify irregular signals and potentially aid in patient diagnoses. Although the current model only detects preliminary events and performs simple classifications, improved models and algorithms will eventually lead to better performance and making better decisions. Ultimately, the widespread implementation of wearable systems, coupled with advanced data processing, has the potential to significantly improve the quality of life for patients and advance the field of medicine itself.

References

1. Zhou, Y. *et al.* High-resolution integrated piezoresistive sensors for microfluidic monitoring. *Lab Chip* **21**, 83–92 (2021).

2. Kostopoulou, O., Delaney, B. C. & Munro, C. W. Diagnostic difficulty and error in primary care - A systematic review. *Family Practice* (2008) doi:10.1093/fampra/cmn071.

3. Asher, I. & Pearce, N. Global burden of asthma among children. *Int. J. Tuberc. Lung Dis.* (2014) doi:10.5588/ijtld.14.0170.

4. Yamada, T. *et al.* A stretchable carbon nanotube strain sensor for human-motion detection. *Nat. Nanotechnol.* **6**, 296–301 (2011).

5. Heikenfeld, J. *et al.* Wearable sensors: Modalities, challenges, and prospects. *Lab on a Chip* (2018) doi:10.1039/c7lc00914c.

6. Jeong, H. *et al.* NFC-enabled, tattoo-like stretchable biosensor manufactured by “cut-and-paste” method. in *2017 39th Annual International Conference of the IEEE Engineering in Medicine and Biology Society (EMBC)* 4094–4097 (IEEE, 2017). doi:10.1109/EMBC.2017.8037756.

7. Zamarayeva, A. M. *et al.* Flexible and stretchable power sources for wearable electronics. *Sci. Adv.* **3**, (2017).

8. Keum, K. *et al.* Flexible/Stretchable Supercapacitors with Novel Functionality for Wearable Electronics. *Adv. Mater.* **32**, 2002180 (2020).

9. Kim, J. *et al.* Soft Wearable Pressure Sensors for Beat-to-Beat Blood Pressure Monitoring. *Adv. Healthc. Mater.* **8**, 1900109 (2019).

10. Chu, M. *et al.* Respiration rate and volume measurements using wearable strain sensors. *npj Digit. Med.* **2**, 8 (2019).

11. Kim, T., Park, J., Sohn, J., Cho, D. & Jeon, S. Bioinspired, Highly Stretchable, and Conductive Dry Adhesives Based on 1D-2D Hybrid Carbon Nanocomposites for All-in-One ECG Electrodes. *ACS Nano* (2016) doi:10.1021/acsnano.6b01355.

12. Cheng, S. & Wu, Z. Microfluidic stretchable RF electronics. *Lab Chip* (2010) doi:10.1039/c005159d.

13. Lee, S.-K. *et al.* Stretchable Graphene Transistors with Printed Dielectrics and Gate Electrodes. *Nano Lett.* **11**, 4642–4646 (2011).

14. Xu, S. *et al.* Soft Microfluidic Assemblies of Sensors, Circuits, and Radios for the Skin. *Science (80-.).* **344**, 70–74 (2014).

15. Song, E. *et al.* Flexible electronic/optoelectronic microsystems with scalable designs for chronic biointegration. *Proc. Natl. Acad. Sci.* **116**, 15398–15406 (2019).

16. Dagdeviren, C. *et al.* Recent progress in flexible and stretchable piezoelectric devices for mechanical energy harvesting, sensing and actuation. *Extrem. Mech. Lett.* **9**, 269–281 (2016).

17. Wang, S. *et al.* Skin electronics from scalable fabrication of an intrinsically stretchable transistor array. *Nature* **555**, 83–88 (2018).

18. Kim, J. O. *et al.* Network Structure Modification-Enabled Hybrid Polymer Dielectric Film with Zirconia for the Stretchable Transistor Applications. *Adv. Funct. Mater.* **30**, 1906647 (2020).

19. Yu, I., Ye, Y., Moon, S., Lee, S. & Joo, Y. A Bendable, Stretchable Transistor with Aligned Carbon Nanotube Films. *Adv. Mater. Interfaces* **6**, 1900945 (2019).

20. Wang, W. *et al.* Strain-insensitive intrinsically stretchable transistors and circuits. *Nat. Electron.* (2021) doi:10.1038/s41928-020-00525-1.

21. Guo, R., Wang, X., Yu, W., Tang, J. & Liu, J. A highly conductive and stretchable wearable liquid metal electronic skin for long-term conformable health monitoring. *Sci. China Technol. Sci.* **61**, 1031–1037 (2018).

22. Kim, Y. *et al.* All-in-One, Wireless, Stretchable Hybrid Electronics for Smart, Connected, and Ambulatory Physiological Monitoring. *Adv. Sci.* **6**, 1900939 (2019).

23. Votzke, C., Daalkhaijav, U., Menguc, Y. & Johnston, M. L. 3D-Printed Liquid Metal Interconnects for Stretchable Electronics. *IEEE Sens. J.* (2019) doi:10.1109/JSEN.2019.2894405.

24. Niu, S. *et al.* A wireless body area sensor network based on stretchable passive tags. *Nat. Electron.* **2**, 361–368 (2019).

25. Huang, Z. *et al.* Three-dimensional integrated stretchable electronics. *Nat. Electron.* **1**, 473–480 (2018).

26. Li, Y., Liu, W., Deng, Y., Hong, W. & Yu, H. Miura-ori enabled stretchable circuit boards. *npj Flex. Electron.* **5**, 3 (2021).

27. Li, Y. & Yu, H. A Planar Developable Double Corrugation Surface Enabled Stretchable Heart Rate Sensing System. *IEEE Sens. J.* **21**, 16275–16281 (2021).

28. Kong, M. *et al.* Transparent Omni-Directional Stretchable Circuit Lines Made by a Junction-Free Grid of Expandable Au Lines. *Adv. Mater.* (2021) doi:10.1002/adma.202100299.

29. Lin, S. *et al.* A cost-effective and solderability stretchable circuit boards for wearable devices. *Sensors Actuators A Phys.* **331**, 112924 (2021).

30. Rajesh, Ahuja, T. & Kumar, D. Recent progress in the development of nano-structured conducting polymers/nanocomposites for sensor applications. *Sensors and Actuators, B: Chemical* (2009) doi:10.1016/j.snb.2008.09.014.

31. Stassi, S., Cauda, V., Canavese, G. & Pirri, C. F. Flexible tactile sensing based on piezoresistive composites: A review. *Sensors (Switzerland)* (2014) doi:10.3390/s140305296.

32. Niu, X., Peng, S., Liu, L., Wen, W. & Sheng, P. Characterizing and patterning of PDMS-based conducting composites. *Adv. Mater.* (2007) doi:10.1002/adma.200602515.

33. Xu, W. & Allen, M. G. Deformable strain sensors based on patterned MWCNTs/polydimethylsiloxane composites. *J. Polym. Sci. Part B Polym. Phys.* (2013) doi:10.1002/polb.23361.

34. Cho, H. *et al.* Stretchable strain-tolerant soft printed circuit board: a systematic approach for the design rules of stretchable interconnects. *J. Inf. Disp.* **2020**, 41–47 (2019).

35. Pegan, J. D. *et al.* Skin-mountable stretch sensor for wearable health monitoring. *Nanoscale* **8**, 17295–17303 (2016).

36. Kim, J. *et al.* Highly stretchable wrinkled gold thin film wires. *Appl. Phys. Lett.* (2016) doi:10.1063/1.4941439.

37. Whitesides, G. M. The origins and the future of microfluidics. *Nature* **442**, 368–373 (2006).

38. Han, Z., Li, W., Huang, Y. & Zheng, B. Measuring Rapid Enzymatic Kinetics by Electrochemical Method in Droplet-Based Microfluidic Devices with Pneumatic Valves. *Anal. Chem.* **81**, 5840–5845 (2009).

39. Elizabeth Hulme, S., Shevkoplyas, S. S. & Whitesides, G. M. Incorporation of prefabricated screw,

pneumatic, and solenoid valves into microfluidic devices. *Lab Chip* **9**, 79–86 (2009).

40. Buchenauer, A. *et al.* Micro-bioreactors for fed-batch fermentations with integrated online monitoring and microfluidic devices. *Biosens. Bioelectron.* **24**, 1411–1416 (2009).

41. Clause, K. C., Liu, L. J. & Tobita, K. Directed Stem Cell Differentiation: The Role of Physical Forces. *Cell Commun. Adhes.* **17**, 48–54 (2010).

42. Massenburg, S. S., Amstad, E. & Weitz, D. A. Clogging in parallelized tapered microfluidic channels. *Microfluid. Nanofluidics* **20**, 94 (2016).

43. Unger, M. A. Monolithic Microfabricated Valves and Pumps by Multilayer Soft Lithography. *Science (80-.).* **288**, 113–116 (2000).

44. Jensen, E. C., Grover, W. H. & Mathies, R. A. Micropneumatic Digital Logic Structures for Integrated Microdevice Computation and Control. *J. Microelectromechanical Syst.* **16**, 1378–1385 (2007).

45. Duncan, P. N., Nguyen, T. V. & Hui, E. E. Pneumatic oscillator circuits for timing and control of integrated microfluidics. *Proc. Natl. Acad. Sci.* **110**, 18104–18109 (2013).

46. Wang, X. *et al.* Diaphragm design guidelines and an optical pressure sensor based on MEMS technique. *Microelectronics J.* **37**, 50–56 (2006).

47. Poeggel, S. *et al.* Optical Fibre Pressure Sensors in Medical Applications. *Sensors* **15**, 17115–17148 (2015).

48. Orth, A., Schonbrun, E. & Crozier, K. B. Multiplexed pressure sensing with elastomer membranes. *Lab Chip* **11**, 3810 (2011).

49. Runowski, M., Woźny, P., Stopikowska, N., Guo, Q. & Lis, S. Optical Pressure Sensor Based on the

Emission and Excitation Band Width (fwhm) and Luminescence Shift of Ce 3+ -Doped Fluorapatite—High-Pressure Sensing. *ACS Appl. Mater. Interfaces* **11**, 4131–4138 (2019).

50. Lien, V. & Vollmer, F. Microfluidic flow rate detection based on integrated optical fiber cantilever. *Lab Chip* **7**, 1352 (2007).

51. Tang, L. *et al.* A smart microfluidic system integrated with pressure sensors and flow sensor based on electrochemical impedance methods. in *2017 IEEE 30th International Conference on Micro Electro Mechanical Systems (MEMS)* 1300–1303 (IEEE, 2017). doi:10.1109/MEMSYS.2017.7863657.

52. Liu, W. *et al.* Piezoresistive Pressure Sensor Based on Synergistical Innerconnect Polyvinyl Alcohol Nanowires/Wrinkled Graphene Film. *Small* **14**, 1704149 (2018).

53. Lipomi, D. J. *et al.* Skin-like pressure and strain sensors based on transparent elastic films of carbon nanotubes. *Nat. Nanotechnol.* **6**, 788–792 (2011).

54. Zhang, Y., Howver, R., Gogoi, B. & Yazdi, N. A high-sensitive ultra-thin MEMS capacitive pressure sensor. in *2011 16th International Solid-State Sensors, Actuators and Microsystems Conference* 112–115 (IEEE, 2011). doi:10.1109/TRANSDUCERS.2011.5969151.

55. Lee, J. *et al.* Transparent, Flexible Strain Sensor Based on a Solution-Processed Carbon Nanotube Network. *ACS Appl. Mater. Interfaces* **9**, 26279–26285 (2017).

56. Li, Y.-Q. *et al.* Flexible wire-shaped strain sensor from cotton thread for human health and motion detection. *Sci. Rep.* **7**, 45013 (2017).

57. Wang, D.-Y. *et al.* High performance flexible strain sensor based on self-locked overlapping graphene sheets. *Nanoscale* **8**, 20090–20095 (2016).

58. Shi, G. *et al.* A versatile PDMS submicrobead/graphene oxide nanocomposite ink for the direct ink writing of wearable micron-scale tactile sensors. *Appl. Mater. Today* **16**, 482–492 (2019).

59. Wang, L. *et al.* Polydimethylsiloxane-integratable micropressure sensor for microfluidic chips. *Biomicrofluidics* **3**, 034105 (2009).

60. Grosberg, A., Alford, P. W., McCain, M. L. & Parker, K. K. Ensembles of engineered cardiac tissues for physiological and pharmacological study: Heart on a chip. *Lab Chip* **11**, 4165 (2011).

61. Lind, J. U. *et al.* Instrumented cardiac microphysiological devices via multimaterial three-dimensional printing. *Nat. Mater.* **16**, 303–308 (2017).

62. Czirok, A. *et al.* Optical-flow based non-invasive analysis of cardiomyocyte contractility. *Sci. Rep.* **7**, 10404 (2017).

63. Baldwin, A., Hudson, T. & Meng, E. A calorimetric flow sensor for ultra-low flow applications using electrochemical impedance. in *2018 IEEE Micro Electro Mechanical Systems (MEMS)* 361–364 (IEEE, 2018). doi:10.1109/MEMSYS.2018.8346562.

64. Tang, M. *et al.* Simple and convenient microfluidic flow rate measurement based on microbubble image velocimetry. *Microfluid. Nanofluidics* **23**, 118 (2019).

65. Etxebarria, I., Elizalde, J. & Pacios, R. Smart monolithic integration of inkjet printed thermal flow sensors with fast prototyping polymer microfluidics. *Smart Mater. Struct.* **25**, 085022 (2016).

66. Etxebarria, J. *et al.* Low cost polymeric on-chip flow sensor with nanoliter resolution. *Sensors Actuators B Chem.* **235**, 188–196 (2016).

67. Zarifi, M. H., Sadabadi, H., Hejazi, S. H., Daneshmand, M. & Sanati-Nezhad, A. Noncontact and Nonintrusive Microwave-Microfluidic Flow Sensor for Energy and Biomedical Engineering. *Sci.*

Rep. **8**, 139 (2018).

68. Wang, Z., Volinsky, A. A. & Gallant, N. D. Crosslinking effect on polydimethylsiloxane elastic modulus measured by custom-built compression instrument. *J. Appl. Polym. Sci.* **131**, n/a-n/a (2014).

69. Bradski, G. The OpenCV Library. *Dr Dobbs J. Softw. Tools* (2000).

70. Lacour, S. P., Chan, D., Wagner, S., Li, T. & Suo, Z. Mechanisms of reversible stretchability of thin metal films on elastomeric substrates. *Appl. Phys. Lett.* **88**, 204103 (2006).

71. Oldfrey, B., Jackson, R., Smitham, P. & Miodownik, M. A Deep Learning Approach to Non-linearity in Wearable Stretch Sensors. *Front. Robot. AI* **6**, (2019).

72. Christoforidis, T., Werner, E. M., Hui, E. E. & Eddington, D. T. Vacuum pressure generation via microfabricated converging-diverging nozzles for operation of automated pneumatic logic. *Biomed. Microdevices* **18**, 74 (2016).

73. Ge, G. *et al.* A flexible pressure sensor based on rGO/polyaniline wrapped sponge with tunable sensitivity for human motion detection. *Nanoscale* **10**, 10033–10040 (2018).

74. Gong, S. *et al.* A wearable and highly sensitive pressure sensor with ultrathin gold nanowires. *Nat. Commun.* **5**, 3132 (2014).

75. Lee, S. *et al.* A transparent bending-insensitive pressure sensor. *Nat. Nanotechnol.* **11**, 472–478 (2016).

76. Liu, S., Shah, D. S. & Kramer-Bottiglio, R. Highly stretchable multilayer electronic circuits using biphasic gallium-indium. *Nat. Mater.* (2021) doi:10.1038/s41563-021-00921-8.

77. Kim, S., Oh, J., Jeong, D. & Bae, J. Direct Wiring of Eutectic Gallium-Indium to a Metal Electrode

for Soft Sensor Systems. *ACS Appl. Mater. Interfaces* (2019) doi:10.1021/acsami.9b05363.

78. van der Helm, E. & Walker, M. P. Overnight therapy? The role of sleep in emotional processing. *Psychol. Bull.* (2009).

79. Rasch, B. & Born, J. About sleep's role in memory. *Physiol. Rev.* (2013) doi:10.1152/physrev.00032.2012.

80. Hobson, J. A., Mccarley, R. W. & Wyzinski, P. W. Sleep cycle oscillation: Reciprocal discharge by two brainstem neuronal groups. *Science (80-.).* (1975) doi:10.1126/science.1094539.

81. Carskadon, M. A. & Dement, W. C. Chapter 2 – Normal Human Sleep : An Overview. *Princ. Pract. Sleep Med. Fifth Ed.* (2011).

82. Iber, C., Ancoli-Israel, S., Chesson, A. L. & Quan, S. F. The new sleep scoring manual - The evidence behind the rules. *Journal of Clinical Sleep Medicine* (2007) doi:10.5664/jcsm.26812.

83. Mahowald, M. W. & Schenck, C. H. Insights from studying human sleep disorders. *Nature* (2005) doi:10.1038/nature04287.

84. Stickgold, R. & Walker, M. P. Sleep-dependent memory triage: Evolving generalization through selective processing. *Nature Neuroscience* (2013) doi:10.1038/nn.3303.

85. Vgontzas, A. N., Bixler, E. O. & Chrousos, G. P. Metabolic disturbances in obesity versus sleep apnoea: The importance of visceral obesity and insulin resistance. in *Journal of Internal Medicine* (2003). doi:10.1046/j.1365-2796.2003.01177.x.

86. Irwin, M. R. Why sleep is important for health: A psychoneuroimmunology perspective. *Annu. Rev. Psychol.* (2015) doi:10.1146/annurev-psych-010213-115205.

87. Franklin, K. A. & Lindberg, E. Obstructive sleep apnea is a common disorder in the population-A

review on the epidemiology of sleep apnea. *Journal of Thoracic Disease* (2015) doi:10.3978/j.issn.2072-1439.2015.06.11.

88. Schenck, C. H. & Mahowald, M. W. REM sleep behavior disorder: Clinical, developmental, and neuroscience perspectives 16 years after its formal identification in SLEEP. *Sleep* (2002) doi:10.1093/sleep/25.2.120.

89. Iranzo, A., Santamaria, J. & Tolosa, E. Idiopathic rapid eye movement sleep behaviour disorder: Diagnosis, management, and the need for neuroprotective interventions. *The Lancet Neurology* (2016) doi:10.1016/S1474-4422(16)00057-0.

90. Korkalainen, H. *et al.* Deep learning enables sleep staging from photoplethysmogram for patients with suspected sleep apnea. *Sleep* (2020) doi:10.1093/sleep/zsaa098.

91. Zhao, X. & Sun, G. A multi-class automatic sleep staging method based on photoplethysmography signals. *Entropy* (2021) doi:10.3390/e23010116.

92. Habib, A. *et al.* Performance of a Convolutional Neural Network Derived from PPG Signal in Classifying Sleep Stages. *IEEE Trans. Biomed. Eng.* **XX**, 1–15 (2022).

93. Sekkal, R. N., Bereksi-Reguig, F., Ruiz-Fernandez, D., Dib, N. & Sekkal, S. Automatic sleep stage classification: From classical machine learning methods to deep learning. *Biomed. Signal Process. Control* **77**, 103751 (2022).

94. Jordan, A. S., McSharry, D. G. & Malhotra, A. Adult obstructive sleep apnoea. *Lancet* **383**, 736–747 (2014).

95. White, D. P. Pathogenesis of Obstructive and Central Sleep Apnea. *https://doi.org/10.1164/rccm.200412-1631SO* **172**, 1363–1370 (2012).

96. Du-Yan, G., Jia-Xing, W., Yan, W. & Xuan-Yu, L. Convolutional neural network is a good technique for sleep staging based on HRV: A comparative analysis. *Neurosci. Lett.* **779**, 136550 (2022).

97. Wei, R., Zhang, X., Wang, J. & Dang, X. The research of sleep staging based on single-lead electrocardiogram and deep neural network. *Biomed. Eng. Lett.* (2018) doi:10.1007/s13534-017-0044-1.

98. Liu, M. *et al.* Gated Transformer Networks for Multivariate Time Series Classification. (2021) doi:10.48550/arxiv.2103.14438.

99. Ahmed, S. *et al.* Transformers in Time-series Analysis: A Tutorial. (2022) doi:10.48550/arxiv.2205.01138.

100. Lim, B., Arık, S., Loeff, N. & Pfister, T. Temporal Fusion Transformers for Interpretable Multi-horizon Time Series Forecasting. *Int. J. Forecast.* **37**, 1748–1764 (2019).

101. Geng, Z., Chen, Z., Meng, Q. & Han, Y. Novel Transformer Based on Gated Convolutional Neural Network for Dynamic Soft Sensor Modeling of Industrial Processes. *IEEE Trans. Ind. Informatics* **18**, 1521–1529 (2022).